MOLECULAR BIOLOGY

VGLL3 modulates chemosensitivity through promoting DNA double-strand break repair

Wei Wu^{1,2}†, Zhenzhen Fan^{1,2}†, Hui Fu^{1,2,3}†, Xiaolu Ma^{4,5,6}†, Dongzhou Wang^{1,2,3}, Hongmei Liu^{4,6}, Chuanchao Zhang², Hui Zheng², Yeran Yang², Honglin Wu^{3,4,6}, Xiuxiu Miao^{1,2,3}, Ruiyuan An^{1,2,3}, Yifei Gong^{1,2,3}, Tie-Shan Tang^{3,4,6}*, Caixia Guo^{1,2,3}*

Transcription cofactor vestigial-like 3 (VGLL3), as a master regulator of female-biased autoimmunity, also functions in tumor development, while the underlying mechanisms remain largely elusive. Here, we report that VGLL3 plays an important role in DNA damage response (DDR). VGLL3 can be recruited to damage sites in a PARylation-dependent manner. VGLL3 depletion impairs the accumulation of RNF8 and RAD51 at sites of DNA damage, leading to reduced homologous recombination efficiency and increased cellular sensitivity to chemotherapeutic drugs. Mechanistically, VGLL3 can prevent CtIP from KLHL15-mediated ubiquitination and degradation through competitive binding with KLHL15 and, meanwhile, stabilize MDC1 by limiting TRIP12-MDC1 but promoting USP7-MDC1 associations for optimal RNF8 signaling initiation. Consistently, VGLL3 depletion delays tumor development and sensitizes the xenografts to etoposide treatment. Overall, our results reveal an unexpected role of VGLL3 in DDR, which is distinct from its transcriptional cofactor function and not conserved among VGLL family members.

Copyright © 2024 The Authors, some rights reserved; exclusive licensee American Association for the Advancement of Science. No claim to original U.S.
Government Works.
Distributed under a Creative Commons Attribution
NonCommercial
License 4.0 (CC BY-NC).

INTRODUCTION

Vestigial-like 3 (VGLL3) is a member of the VGLL family that contains a conserved TONDU motif (TDU), a region essential for binding with TEA domain-containing transcription factors (TEADs) (1). Distinct from other VGLL family members, VGLL3 also contains a glutamate-rich (E-rich) motif at the N terminus and a histidine-rich (H-rich) motif at the C terminus, which are speculated to mediate VGLL3 to undergo liquid-liquid phase separation in mouse myofibroblasts and localize to nuclear speckles, respectively (2, 3). As a candidate female-biased immune regulator, the elevated VGLL3 expression is associated with inflammatory diseases, especially female-biased autoimmune diseases (4-6). Recently, emerging evidence implicated a role of VGLL3 in tumor development (7, 8). VGLL3 was reported to associate with cancer progression by promoting tumor cell proliferation or motility, with its expression positively correlated with poor prognosis in multiple types of human cancers, including breast, ovarian, colon, and gastric cancers (8-10). Paradoxically, a tumor suppressor role of VGLL3 was also reported in estrogen receptor (ER)-positive breast cancers, in which VGLL3 is essential in mediating Hippo/Yes-associated protein (YAP) signaling to repress ESR1 (encoding ER α) expression (7). Moreover, VGLL3 was reported to confer therapeutic resistance to TEAD-YAP blockade through functioning as a transcription coactivator to induce the expression of YAP-suppressed genes (11). Nevertheless, unlike its homolog VGLL4 (12, 13), how VGLL3 functions in tumor development remains largely obscure.

¹China National Center for Bioinformation, Beijing 100101, China. ²Beijing Institute of Genomics, Chinese Academy of Sciences, Beijing 100101, China. ³University of Chinese Academy of Sciences, Beijing 100049, China. ⁴Key Laboratory of Organ Regeneration and Reconstruction'State Key Laboratory of Membrane Biology, Institute of Zoology, Chinese Academy of Sciences, Beijing 100101, China. ⁵College of Biomedical Engineering, Taiyuan University of Technology, Taiyuan 030024, China. ⁶Beijing Institute for Stem Cell and Regenerative Medicine, Beijing 100101, China. *Corresponding author. Email: guocx@big.ac.cn (C.G.); tangtsh@ioz.ac.cn (T.-S.T) †These authors contributed equally to this work.

DNA double-strand breaks (DSBs) are one of the most deleterious types of DNA lesions, which can result in mutagenic events or cell death if left unrepaired or repaired inappropriately (14, 15). Upon formation of DSBs, the kinase ATM is activated, which rapidly phosphorylates H2AX at serine-139 (16). Mediator of DNA damage checkpoint protein 1 (MDC1) is recruited to DSB sites through binding with γ H2AX followed by recruitment of ubiquitin ligases RNF8-RNF168 to break sites (17–20). RNF8-RNF168–triggered chromatin ubiquitination then promotes engagement of key DNA damage response (DDR) factors, such as 53BP1 and BRCA1 to DSBs (21–23). As a mediator for the recruitment and retention of DDR factors in chromatin regions flanking DSBs, the level of MDC1 is under stringent regulation (24), whose aberrant reduction was observed in a substantial proportion of carcinomas (25, 26).

In general, DSBs are mainly repaired by nonhomologous end joining (NHEJ) and homologous recombination (HR). While NHEJ is active throughout interphase to facilitate the direct end ligation in an error-prone fashion, HR is restricted to the S-G₂ phases of the cell cycle to allow for error-free repair by using a homologous sister chromatid as a template (16, 27). DSB end resection is an essential process in HR, which is initiated by the MRE11-RAD50-NBS1 (MRN) complex with CtBP-interacting protein (CtIP) followed by extension with multiple nucleases, including exonuclease 1 (EXO1), to generate a long 3' single-stranded DNA (ssDNA) tail for replication protein A (RPA) and RAD51 loading. Given its essential role in DNA end resection, CtIP level is also under strict regulation (16, 28), although the underlying mechanism(s) remain to be further determined.

Here, we report that VGLL3 can be recruited to DSBs in a PARylation- and chromodomain helicase DNA binding protein 4 (CHD4)-dependent manner. VGLL3 associates with KLHL15, an E3 ubiquitin ligase adaptor, to prevent CtIP from proteasomal degradation. VGLL3 also associates with MDC1 to enhance the MDC1-USP7 interaction and to limit the interaction between MDC1 and thyroid hormone receptor interactor 12 (TRIP12), a known E3 ubiquitin ligase for USP7 (29). Depletion of VGLL3

down-regulates the expression of CtIP and MDC1 at the protein level, impairing the recruitment of multiple DDR factors to DSBs. As a functional consequence, VGLL3 deficiency impairs HR repair and sensitizes cells to multiple DSB-inducing agents. Consistently, targeting VGLL3 inhibits tumor growth and sensitizes xenografted tumors to etoposide (ETO) treatment. Together, our data reveal that VGLL3 can function as a DDR regulator that is essential for optimal initial DDR signaling and DSB end resection, which is independent of its roles in transcriptional regulation.

RESULTS

VGLL3 accumulates at DSBs in a PARylation- and CHD4-dependent fashion

To determine whether VGLL3 plays a role in DDR, green fluorescent protein (GFP)-tagged VGLL3 was expressed in U2OS cells followed by laser microirradiation. We found that GFP-VGLL3 could be recruited to laser-induced DNA damage sites within 1 min, with an accumulation peak at around 5 min followed by a modest decrease (Fig. 1, A and B). Pretreatment with ABT-888 [a poly(ADPribose) polymerase (PARP) inhibitor (PARPi)] but not KU55933 [ataxia telangiectasia mutated (ATM) inhibitor] or AZD6738 [ataxiatelangiectasia mutated and Rad3-related (ATR) inhibitor] could significantly block the accrual of GFP-VGLL3 (Fig. 1, C to E), indicating that PARylation is required for its enrichment at damage sites. However, VGLL3 failed to associate with PAR chains (fig. S1A), hinting that its recruitment is not mediated through direct binding with PARylated proteins. To identify the potential factors mediated VGLL3 recruitment, nuclear extracts from 293T cells expressing SFB-VGLL3 were undergone a tandem affinity purification. Proteins associated with VGLL3 were identified by mass spectrometry analysis (fig. S1B and table S1), which include CHD4, DEAD-Box Helicase 5 (DDX5), and DDX17. As a core subunit of the nucleosome remodeling and histone deacetylase complex, CHD4 is known to be recruited to DNA damage sites in a PARylation-dependent manner. To confirm their interaction, the chromatin fractions of 293T cells expressing Flag-VGLL3 and GFP-CHD4 were harvested for co-immunoprecipitation (Co-IP). We found that GFP-CHD4 was associated with Flag-VGLL3, and their association was enhanced upon ETO treatment (Fig. 1F). Moreover, their endogenous association was also confirmed (Fig. 1G). We then examined how CHD4 modulates VGLL3 recruitment and found that CHD4 depletion reduces VGLL3 accumulation at damage sites (Fig. 1H and fig. S1C), with a lower extent than that caused by PARPi. This result hints to a possibility that PARylation can also promote VGLL3 recruitment through a CHD4-independent fashion. Because PARvlationdependent chromatin relaxation at damage sites allows accessibility of DDR proteins, including CHD4 (30, 31), we then examined whether it also promotes VGLL3 recruitment by depleting CHD1L/ ALC1 in DR-GFP U2OS cells stably expressing Flag-VGLL3 (fig. S1D). CHD1L/ALC1 is a chromatin remodeling enzyme and has been shown to induce the initial chromatin relaxation to facilitate the recruitment of CHD4 and other factors to DSBs (31, 32). Our chromatin immunoprecipitation (ChIP)-quantitative polymerase chain reaction (qPCR) analysis revealed that, similar to CHD4, VGLL3 enrichment at the I-SceI-induced DSBs was significantly impaired upon CHD1L/ALC1 depletion, supporting a role of PARylation-dependent chromatin relaxation in VGLL3 recruitment to DSBs (Fig. 1I). Meanwhile, VGLL3 knockdown had no effect on

CHD4 recruitment (fig. S1E). We also confirmed the interactions between VGLL3 and DDX5 or DDX17 through Co-IP (fig. S1F). However, depletion of either DDX5 or DDX17 had no effect on GFP-VGLL3 recruitment (fig. S1, G and H).

We further generated a series of VGLL3 deletion mutants that span the entire VGLL3 protein (fig. S1I) to determine which domain in VGLL3 mediates its association with CHD4. The result showed that deletion of the E-rich motif ($\Delta 2$ mutant) abolishes its association with CHD4 (Fig. 1J). This deletion also blocked VGLL3 recruitment after microirradiation (fig. S1, J and K). While the recruitment of other VGLL3 mutants, including the Δ 3 mutant with deletion of the TDU domain, showed no obvious reduction. To further confirm that VGLL3 can be recruited to DSB sites through the E-rich motif, DR-GFP U2OS cells expressing wild type (WT) or $\Delta 2$ Flag-VGLL3 were infected with I-SceI-containing lentivirus followed by ChIP-qPCR analysis. A clear enrichment of WT VGLL3 at the I-SceI-induced DSBs was observed (Fig. 1K), while the deletion of the E-rich motif abrogated this enrichment. These results indicate that VGLL3 can be recruited to DSBs through its E-rich motif, dependent of PARylation-mediated chromatin relaxation and association with CHD4.

VGLL3 loss impairs HR and sensitizes cells to chemotherapeutic drugs

Micronuclei formation is widely used to monitor genotoxic events and chromosomal instability. We first determined whether VGLL3 silencing would affect the micronucleus formation frequency. The results showed that the depletion of VGLL3 but not VGLL4 in U2OS cells results in a higher proportion of cells with micronuclei in the absence or presence of bleomycin treatment (Fig. 2A and fig. S2A). A same change tendency was also demonstrated in MDA-MB-231 cells (Fig. 2A), suggesting that loss of VGLL3 expression specifically results in genome instability. To further elucidate the role of VGLL3 in DDR, we established VGLL3 knockout (KO) U2OS and MDA-MB-231 cell lines, and loss of VGLL3 was confirmed by immunoblotting with an anti-VGLL3 antibody whose specificity was determined (fig. S2B) and Sanger sequencing (fig. S2C). We then treated VGLL3 WT and KO U2OS cells with ETO and examined the γH2AX signal at different time points post treatment. VGLL3 KO caused an obvious increase in γH2AX signal under unperturbed condition (Fig. 2B). After ETO exposure, γH2AX signal increased notably at 0.5 hours after treatment and then gradually decreased following recovery. Notably, loss of VGLL3 caused a delayed clearance of yH2AX signal compared to the WT control, which could be reversed by complementing with GFP-VGLL3 through lentivirus infection (Fig. 2B), suggesting a potential role of VGLL3 in DSB repair.

We then examined the effect of VGLL3 depletion on HR and NHEJ, two major DSB repair pathways in eukaryotic cells. U2OS DR-GFP or EJ5-GFP reporter cells were used to measure the repair rates of I-SceI-induced DSBs in chromosomal DNA by HR or NHEJ, respectively. Depletion of VGLL3 decreased the frequency of HR (Fig. 2C) but not NHEJ (Fig. 2D). In addition, the reduced HR efficiency caused by VGLL3 loss could be fully rescued by complementing with Flag-VGLL3 (Fig. 2E). We noticed that VGLL3 depletion did not affect cell cycle distribution (fig. S2D). Meanwhile, the depletion of VGLL4 had no obvious effect on HR efficiency (fig. S2E). In addition, the depletion of VGLL3 in U2OS-MMEJ reporter cells also decreased the frequency of MMEJ (fig. S2F), a

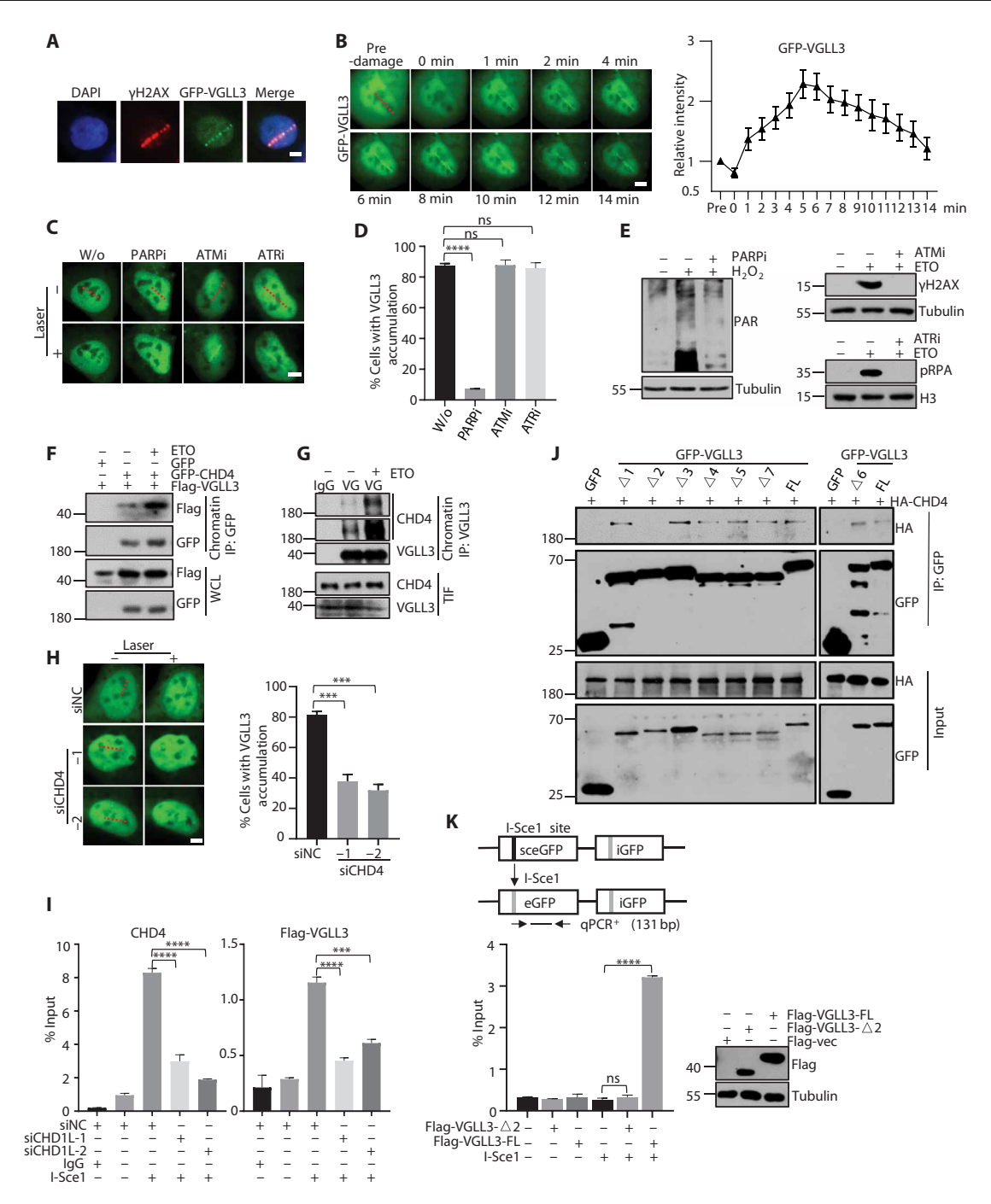


Fig. 1. VGLL3 is recruited to DSBs depending on PARylation and CHD4. (A and B) U2OS cells stably expressing GFP-VGLL3 were microirradiated. (A) Representative images. Scale bars, 2 μm. (B) Left: Representative live cell images. Right: The intensity of fluorescence at damage sites was quantified and presented as means \pm SD from 10 cells. (C) U2OS cells expressing GFP-VGLL3 were pretreated with the indicated inhibitors before microirradiation. (D) Proportion of cells with VGLL3 accumulation was quantified. Data were derived from at least 20 cells per replicate and presented as means \pm SEM from three experiments. (E) Immunoblotting (IB) validates inhibitor efficiencies. (F) Chromatin fractions of 293T cells expressing Flag-VGLL3 and GFP-CHD4 were harvested for immunoprecipitation (IP). WCL, whole-cell lysis. (G) Chromatin fractions (Triton X-100-insoluble fractions) of 293T cells were harvested for IP with anti-VGLL3 antibody. (H) CHD4-depleted U2OS cells were transfected with GFP-VGLL3 followed by microirradiation. Proportion of cells with VGLL3 accumulation was quantified. Data were derived from analysis of at least 25 cells per replicate and presented as means \pm SEM from three experiments. (I) U2OS-DR-GFP or U2OS-DR-GFP cells expressing Flag-VGLL3 were transfected with siCHD1L. Chromatin immunoprecipitation (ChIP)—quantitative polymerase chain reaction (qPCR) at DSBs was performed using anti-Flag or anti-CHD4 antibodies. A representative result from at least three individual experiments is shown. Data are presented as means \pm SEM from at least three replicates per experiment. (J) 293T cells were transfected with hemagglutinin (HA)—CHD4 and GFP-VGLL3 deletions for co-IP. (K) U2OS DR-GFP cells expressing Flag-VGLL3 wild type (WT) or Δ 2 mutant were harvested for ChIP-PCR. Enrichment of VGLL3 at DSBs was measured, and a representative result from at least two individual experiments is shown (bottom left). Data are presented as means \pm SEM from at least three replicates per experiment, unpaired t test.

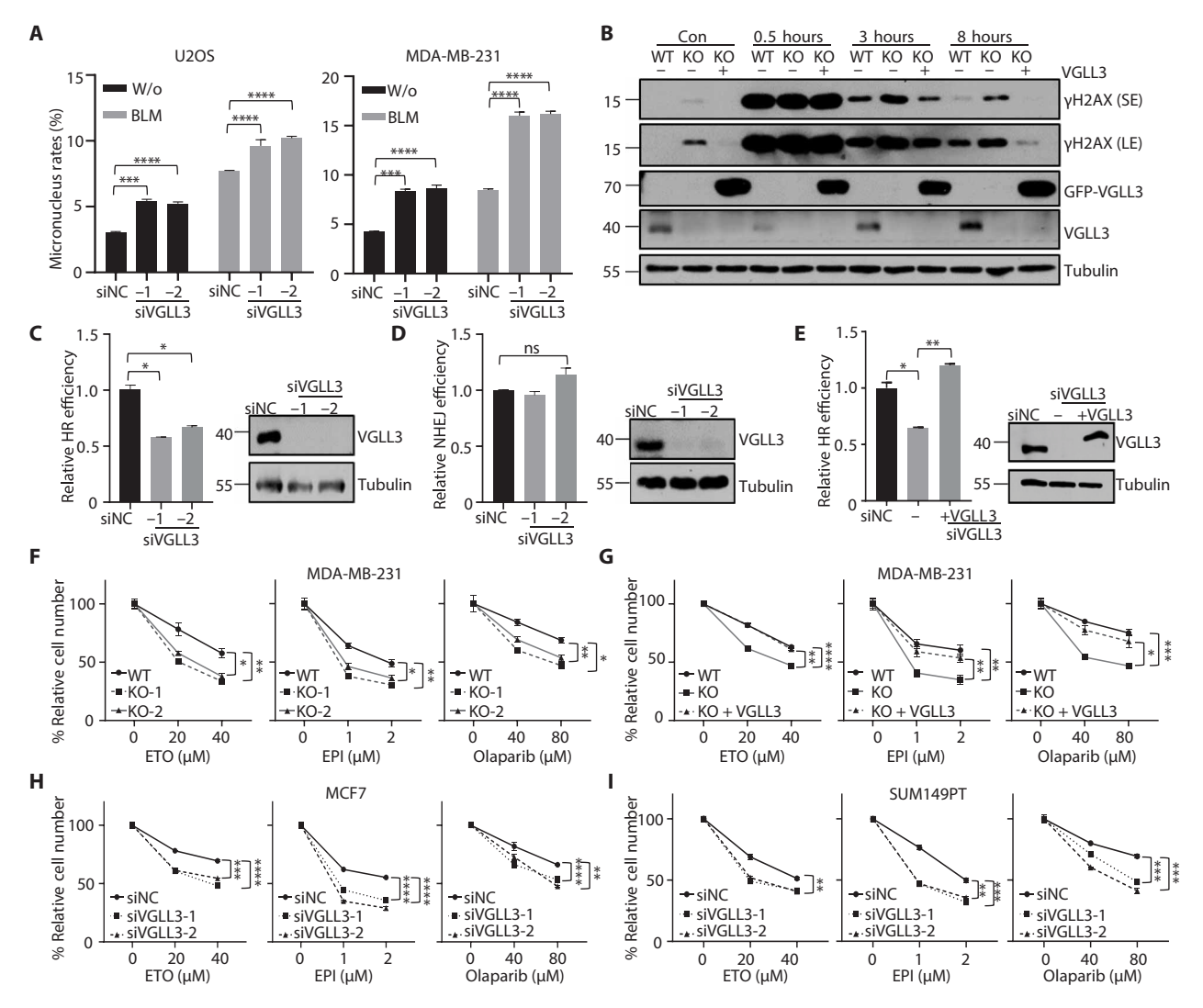


Fig. 2. Loss of VGLL3 impairs HR and sensitizes cells to DNA damage agents. (A) Percentage of VGLL3-depleted U2OS (left) or MDA-MB-231 (right) cells containing one or more micronuclei after treatment with bleomycin (4 μg/ml) for 2 hours. Data are presented as means \pm SEM from three experiments, unpaired t test. (B) VGLL3-KO and GFP-VGLL3 complemented U2OS cells were treated with 20 μM ETO for 2 hours followed by recovery for 0.5, 3, and 8 hours. The levels of γH2AX were analyzed by IB. (C and D) Cells bearing HR (C) or NHEJ (D) reporter were transfected with siVGLL3s. The efficiencies of HR or NHEJ were analyzed by flow cytometry. A representative result from at least three individual experiments is shown (left). Data are presented as means \pm SEM from at least two replicates per experiment, unpaired t test. VGLL3 expression was examined by IB (right). (E) Cells bearing HR reporter were transfected with siVGLL3s and complemented with Flag-VGLL3. The HR efficiencies were analyzed. A representative result from two individual experiments is shown (left). Data are presented as above. VGLL3 expression was examined by IB (right). (F to I) Sensitivity assays of VGLL3 KO or depleted MDA-MB-231 (F), MCF7 (H), SUM149PT (I) cells, or GFP-VGLL3 complemented MDA-MB-231 cells (G). Cells were treated with indicated doses of EPI or ETO for 24 hours, Olaparib for 72 hours. CCK8 assay was performed to detect the survival rate of cells. A representative result from three individual experiments is shown. Data are presented as means \pm SEM from three replicates per experiment, unpaired t test. *P < 0.00, *P < 0.00, *P < 0.001, *P < 0.0001.

minor DSB repair pathway. Moreover, *VGLL3* KO MDA-MB-231 and U2OS cells exhibited increased sensitivity to multiple DSB-inducing drugs, including camptothecin (CPT), ETO, epirubicin (EPI), and olaparib (Fig. 2F and fig. S2, G and H). Also, complementing with WT VGLL3 could reverse the cellular sensitivity to these drugs (Fig. 2G). However, loss of VGLL3 did not sensitize MDA-MB-231 cells to ICRF-193 (fig. S2G), a drug that induced DNA damage is predominantly repaired by NHEJ pathway (33). Furthermore, knockdown of VGLL3 in MCF7 (ER-positive breast cancer cells) and SUM149PT (BRCA1-deficient breast cancer cells) also sensitized the cells to ETO, EPI, and olaparib treatments

(Fig. 2, H and I, and fig. S2I). These results indicate that VGLL3 promotes HR.

VGLL3 regulates CtIP protein level

To investigate how VGLL3 facilitates the HR process, we examined whether VGLL3 deficiency affects the focus formation of several key HR factors upon ETO exposure. We found that loss of VGLL3 causes a significant reduction in RAD51, BRCA1, and RPA focus formation (Fig. 3, A to C, and fig. S3A), which could be fully rescued by complementing with WT VGLL3. Notably, depletion of VGLL3 also reduced ETO-induced 53BP1 focus formation in U2OS cells

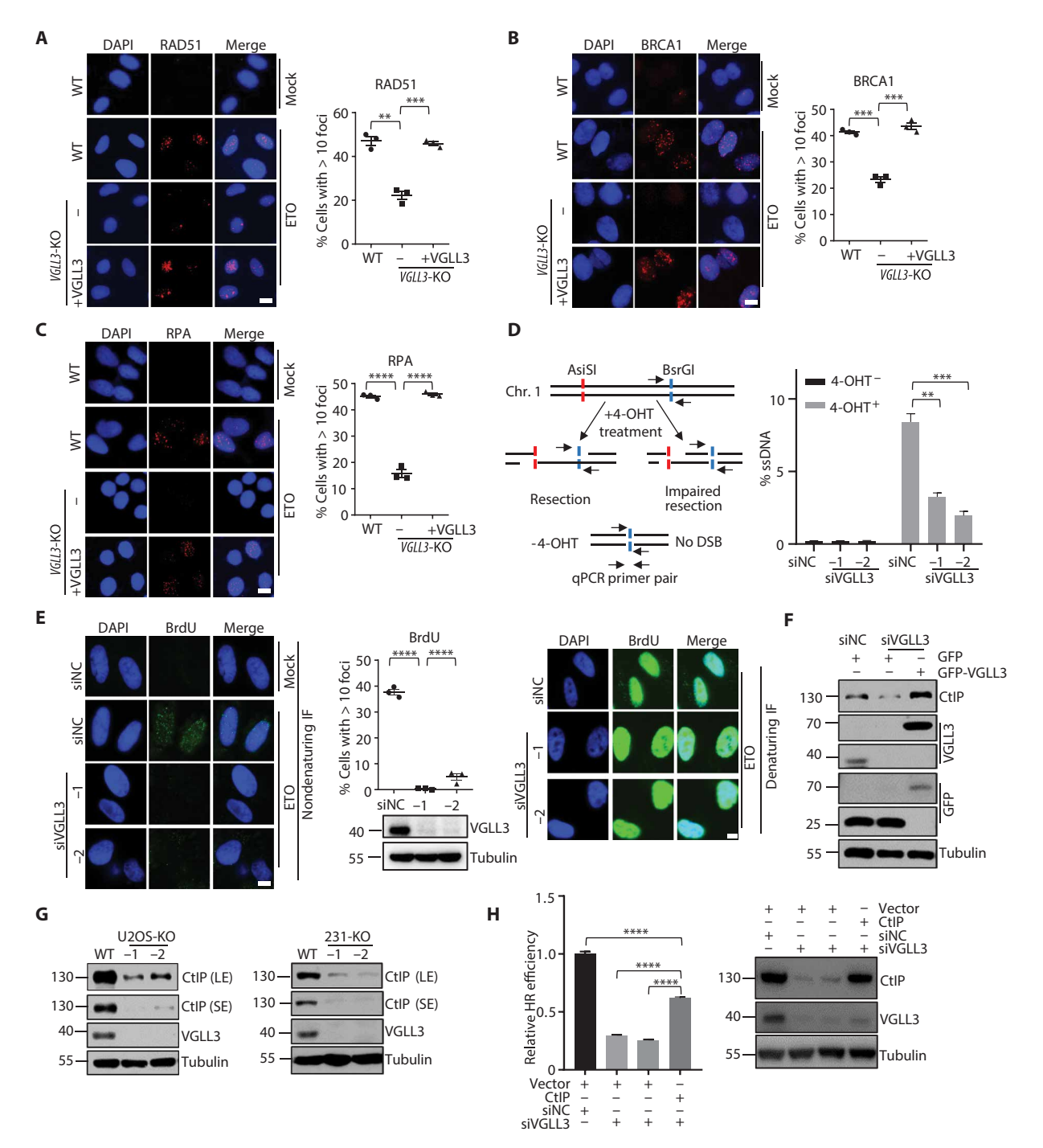


Fig. 3. VGLL3 regulates CtIP protein level. (**A** to **C**) *VGLL3*-KO-1 U2OS cells stably expressing GFP-VGLL3 were treated with ETO (20 μM) for 1 hour and recovered for 3 hours before immunofluorescence (IF) for RAD51, BRCA1, and RPA. Representative images are shown (left). Scale bar, 10 μm. Percentages of cells with >10 foci were quantified (more than 200 cells per replicate) (right). Data are presented as means \pm SEM from three experiments, unpaired *t* test. (**D**) Diagram of the DNA end resection detection system (left). U2OS-ER-AsiSI cells transfected with siVGLL3 were treated with 4-OHT for 6 hours followed by qPCR with the indicated primers amplifying regions including the positions at 364-base pair downstream from the DSB. A representative result from two individual experiments is shown (right). Data are presented as means \pm SEM from at least two replicates per experiment, unpaired *t* test. (**E**) U2OS cells transfected with siVGLL3 were labeled with 10 μM BrdU for 48 hours, followed by treatment with ETO. Representative images under native conditions are shown (left). Percentage of cells with >10 BrdU foci was quantified, with data representing means \pm SEM from three experiments (top middle). Knockdown efficiencies are examined by IB (bottom middle). Representative images of BrdU staining after denaturation with 2 M HCl are shown (right). (**F**) U2OS cells stably expressing GFP-VGLL3 were transfected with siVGLL3 followed by IB. (**G**) CtIP protein expression was examined in *VGLL3* KO U2OS or MDA-MB-231 cells. LE, long exposure; SE, short exposure. (**H**) U2OS DR-GFP cells infected with pNL-cytomegalovirus-CtIP lentivirus were depleted of VGLL3 followed by HR analysis. A representative result from two individual experiments is shown. Data are presented as means \pm SEM from at least three replicates per experiment. Protein expression was examined by IB. ***P < 0.001, ****P < 0.0001.

(fig. S3B). Because DNA end resection is a prerequisite for assembly of RPA-coated ssDNAs, we then examined whether the depletion of VGLL3 impairs this process. We quantitated ssDNA around DSBs by using an established U2OS cell line stably expressing ER-AsiSI (the AsiSI endonuclease fused to the ER) (28) and confirmed that DNA end resection was impaired in VGLL3-depleted cells (Fig. 3D and fig. S3C). To further support the notion that VGLL3 is required for optimal DNA end resection, U2OS cells transfected with siRNA negative control (siNC) or siVGLL3 were labeled with 5-bromo-2'-deoxyuridine (BrdU), followed by ETO treatment. The results of immunofluorescence analysis showed that VGLL3 depletion impaired BrdU foci under native conditions, which detects ss-DNAs generated by end resection, when the entire nuclear DNAs were more or less evenly labeled with BrdU as detected under denaturing conditions (Fig. 3E).

To understand how VGLL3 depletion interferes with DNA end resection, we examined its effects on the protein expression of several HR core factors. VGLL3 depletion caused a notable reduction in the protein abundance of CtIP (fig. S3D), which could be rescued by supplementing with GFP-VGLL3 (Fig. 3F). Although VGLL3 depletion did not affect the protein expression of BRCA1, RAD51, MRE11, EXO1, and RPA32 (fig. S3D). We found that CtIP protein level was also remarkably decreased in VGLL3 KO U2OS or MDA-MB-231 cells (Fig. 3G) and VGLL3-depleted 293T, MDA-MB-231, MCF7, A375, and SKOV3 cells (fig. S3E), suggesting that it is a general phenomenon for VGLL3-regulated CtIP level. Moreover, the abundance of chromatin-bound CtIP was also reduced upon VGLL3 depletion in U2OS cells with or without ETO treatment (fig. S3F). To determine whether VGLL3 regulates HR and drug sensitivity through modulating CtIP protein level, we infected VGLL3-depleted U2OS DR-GFP or U2OS cells with CtIP-expressing lentivirus. We found that ectopically expressing CtIP could significantly but not fully rescue the HR defect and the cellular sensitivity to ETO and EPI (Fig. 3H and fig. S3G), hinting that VGLL3 depletion might also affect the functions of other potential DDR factors.

VGLL3 prevents CtIP from KLHL15-mediated proteasomal degradation

To understand how loss of VGLL3 reduces CtIP abundance, we performed qPCR analysis and found that VGLL3 depletion in U2OS cells did not affect *CtIP* mRNA expression (fig. S4A). Although the effect of VGLL3 depletion on CtIP protein abundance could be largely blocked by the addition of MG132 (a proteasome inhibitor) but not chloroquine (an autophagy inhibitor) (Fig. 4A), suggesting that VGLL3 regulates CtIP protein level through inhibiting its proteasomal degradation. We then examined whether VGLL3 modulates CtIP ubiquitination. The result showed that VGLL3 knockdown promotes CtIP K48-linked polyubiquitination (Fig. 4B and fig. S4B).

Recent studies have reported that KLHL15, PIN1, APC/C (Cdh1), and SIAH1 can promote CtIP ubiquitination and subsequent degradation (34–36). To determine whether these proteins contribute to the reduction of CtIP in VGLL3-depleted cells, we knocked them down in VGLL3-depleted U2OS cells. Depletion of KLHL15 but not others could restore CtIP level (Fig. 4C and fig. S4C), and depletion of KLHL15 could substantially attenuate the up-regulation of CtIP K48-linked polyubiquitination in siVGLL3-treated cells (Fig. 4D). These results indicate that the accelerated CtIP ubiquitination and proteasomal degradation in VGLL3-depleted cells is largely mediated by KLHL15. Intriguingly, analogous to complementation with CtIP (Fig. 3G and

fig. S3G), KLHL15 depletion could significantly but not fully rescue the HR defect in VGLL3-depleted U2OS DR-GFP cells (Fig. 4E) and the cellular sensitivity to ETO in VGLL3-depleted U2OS cells (fig. S4D), indicating that VGLL3 can regulate HR and drug sensitivity in both KLHL15-CtIP axis-dependent and axis-independent manners.

VGLL3 prevents CtIP from degradation by inhibiting CtIP-KLHL15 binding

To determine how VGLL3 regulates CtIP stability through KLHL15, we first examined whether VGLL3 depletion will increase KLHL15 level. VGLL3 loss did not promote *KLHL15* mRNA expression and protein abundance (fig. S4E). We recently reported that PACMP (a small peptide derived from lncRNA *CTD-2256P15.2*) could also regulate CtIP in a KLHL15-dependent manner (28). To determine whether VGLL3 regulates CtIP stability in a PACMP-dependent fashion, we then examined the effect of VGLL3 depletion on PACMP level by using a previously established U2OS knockin (U2OS-KI) cell line bearing a streptavidin-binding peptide (SBP)–FLAG tag inserted into the C terminus of PACMP. We did not find an obvious change in PACMP level after VGLL3 depletion and vice versa (fig. S4F). In addition, the CtIP level was further reduced after the depletion of both PACMP and VGLL3 compared to their single depletion (fig. S4F), indicating that VGLL3 modulates CtIP level in a PACMP-independent fashion.

To test whether VGLL3 affects CtIP-KLHL15 interaction, SFB-CtIP/GFP-VGLL3 or Flag-VGLL3/GFP-KLHL15 were cotransfected into 293T for Co-IP. We found that VGLL3 associated with KLHL15 but not CtIP (Fig. 4F and fig. S4G). KLHL15 contains an N-terminal BTB-BACK domain and a C-terminal Kelch domain (fig. S4H), the latter is responsible for substrate recognition of Kelchlike proteins. Our Co-IP result showed that the Kelch domain mediated the VGLL3-KLHL15 association (Fig. 4G). Given that the same domain also mediates KLHL15 binding to the C-terminal domain (CTD) of CtIP (CtIP-CTD) to promote CtIP ubiquitination, we then examined whether VGLL3 can inhibit CtIP-KLHL15 interaction by competitive binding. 293T cells cotransfected with GFP-KLHL15 and increased amounts of Flag-VGLL3 plasmids were harvested for Co-IP with GFP beads. The result showed that the amount of co-immunoprecipitated endogenous CtIP exhibited a gradual decrease following the increased amounts of Flag-VGLL3 (Fig. 4H). Because the E-rich motif in VGLL3 was required for VGLL3-KLHL15 association (Fig. 4I), we also performed a competitive binding assay by incubation of glutathione S-transferase (GST)-CtIPCTD with a fixed amount of GFP-KLHL15 in the presence of increased amounts of WT or $\Delta 2$ mutant. The result showed that increasing WT but not Δ2 Flag-VGLL3 could displace GFP-KLHL15 from purified GST-CtIPCTD (fig. S4I). Moreover, unlike WT VGLL3, the $\Delta 2$ mutant failed to rescue the reduced CtIP level in VGLL3 KO cells (Fig. 4J). Because the E-rich motif is also necessary for VGLL3-CHD4 association, we wonder whether CHD4 mediates the VGLL3-KLHL15 association. Co-IP assay showed that CHD4 did not interact with KLHL15 (Fig. 4K), and the depletion of CHD4 did not affect VGLL3-KLHL15 association (Fig. 4K) and CtIP protein expression (Fig. 4L). Overall, these results indicate that VGLL3 protects CtIP from degradation through competitive binding with KLHL15.

VGLL3 promotes MDC1 protein expression and RNF8-RNF168 signaling

To explore how VGLL3 regulates HR in a KLHL15-CtIP axisindependent manner, we first examined the RAD51 focus formation

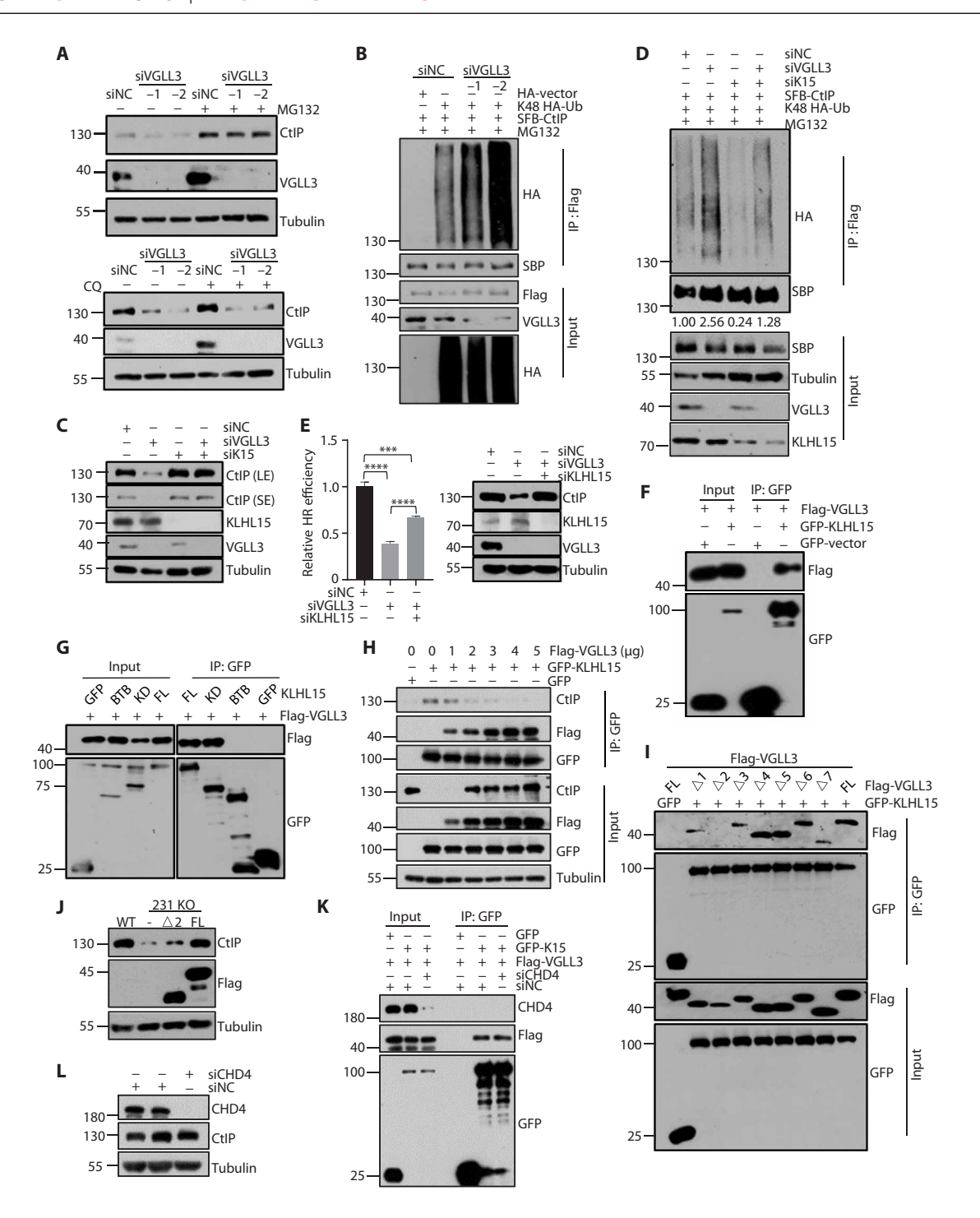


Fig. 4. VGLL3 prevents CtIP from KLHL15-mediated proteasomal degradation. (A) VGLL3-depleted U2OS cells were treated with 10 μM MG132 (top) or chloroquine (bottom) for 8 hours. CtIP protein expression was detected by IB. (B) VGLL3-depleted 293T cells were transfected with K48-only HA-Ub and SFB-CtIP. Thirty-six hours later, cells were treated with MG132 followed by denaturing IP with anti-Flag M2 beads. (C) U2OS cells were treated with indicated siRNAs followed by IB. (D) 293T cells were transfected with indicated siRNAs. Twenty-four hours later, the cells were transfected with SFB-CtIP and K48-only HA-Ub constructs. Thirty-six hours later, cells were treated with MG132 followed by denaturing IP with anti-Flag M2 beads. (E) U2OS DR-GFP cells were transfected with indicated siRNAs. A representative HR result from two individual experiments is shown (left). Data are presented as means \pm SEM from three replicates per experiment, unpaired *t* test. Knockdown efficiencies are examined (right). (F to G) 293T cells expressing Flag-VGLL3 were transfected with GFP-KLHL15 (F) or GFP-KLHL15 truncations (G) followed by IP using anti-GFP beads. (H) 293T cells transfected with GFP-KLHL15 and Flag-VGLL3 deletions were treated with MG132 followed by IP using anti-GFP beads. (J) VGLL3 KO MDA-MB-231 cells infected with Flag-VGLL3 WT or Δ2 lentivirus were harvested for IB. (K) 293T cells depleted of CHD4 were transfected with the indicated constructs, followed by IP with anti-GFP beads. (L) 293T cells transfected with siCHD4 were harvested for IB. (K) 293T cells transfected with siCHD4 were harvested for IB. (K) 293T cells transfected with siCHD4 were harvested for IB. (K) 293T cells transfected with siCHD4 were harvested for IB. (K) 293T cells transfected with siCHD4 were harvested for IB. (K) 293T cells transfected with siCHD4 were harvested for IB. (K) 293T cells transfected with siCHD4 were harvested for IB. (K) 293T cells transfected with siCHD4 were harvested for IB. (K) 293T cells transfected with siCHD4 were harvested

in cells depleted of both KLHL15 and VGLL3 upon ETO treatment. We found that knockdown of KLHL15 fails to fully rescue the foci formation of RAD51 in *VGLL3* KO cells (Fig. 5A). Given that RAD51 focus formation is also modulated by RNF8-RNF168 signaling (*37*–*39*), we then examined whether VGLL3 depletion affects the accumulation of RNF8 and RNF168 at ETO-induced damage sites. The results showed that loss of VGLL3 results in a significant decrease in RNF8 and RNF168 focus formation, which could be rescued by complementing with GFP-VGLL3 (Fig. 5B and fig. S5, A

and B), but not by KLHL15 depletion (fig. S5, C and D), indicating that VGLL3 can also modulate RNF8-RNF168 signaling in a KLHL15-independent fashion. Given that the recruitment of RNF8 to DSB sites was mediated through its association with MDC1, we then examined the effect of VGLL3 loss on MDC1 focus formation. The result showed that the formation of MDC1 foci is significantly impaired upon knockdown of VGLL3 (Fig. 5C). We further found that depletion of VGLL3 also reduced the protein expression of MDC1 in MDA-MB-231 and U2OS cells (Fig. 5D and

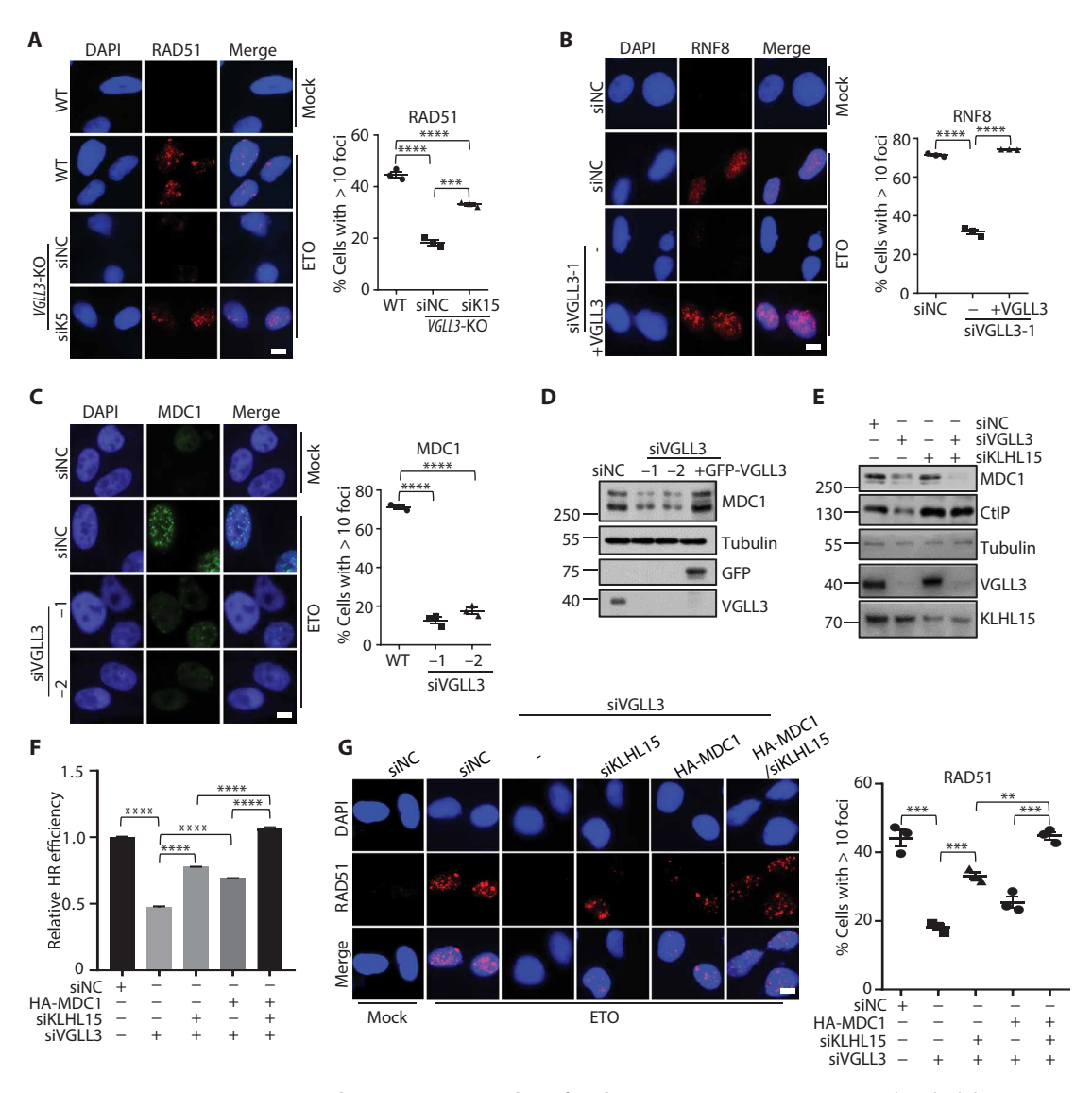


Fig. 5. VGLL3 promotes MDC1 protein expression and RNF8-RNF168 signaling after damage treatment. (A) KLHL15 was knocked down in VGLL3-KO U2OS cells. After 72 hours, cells were treated with ETO (20 μM) for 1 hour and recovered for 3 hours before IF for RAD51. Scale bar, 10 μm. (B) U2OS or U2OS stably expressing GFP-VGLL3 cells were transfected with siVGLL3. After 72 hours, cells were treated with ETO and recovered for 30 min before IF for RNF8. Scale bar, 10 μm. (C) VGLL3-depleted U2OS cells were treated with ETO and recovered for 1 hour before IF for MDC1. Representative images are shown (left). Scale bar, 10 μm. Percentages of cells with >10 foci were quantified (200 cells per replicate) (right). Data are presented as means \pm SEM from three experiments, unpaired t test. (D) U2OS or U2OS stably expressing GFP-VGLL3 cells were transfected with siVGLL3 followed by IB analysis. (E) U2OS cells were transfected with the indicated siRNAs followed by IB. (F) VGLL3-depleted U2OS DR-GFP cells were transfected with siKLHL15, HA-MDC1, or their combination for HR analysis. A representative result from two individual experiments is shown. Data are presented as means \pm SEM from three replicates per experiment, unpaired t test. (G) VGLL3-depleted U2OS cells were transfected with siKLHL15, HA-MDC1, or their combination. The cells were treated with ETO for 1 hour and recovered for 3 hours before IF for RAD51. Representative images are shown (left). Percentages of cells with >10 foci were quantified and presented as above. Scale bar, 10 μm. *P < 0.05, **P < 0.01, **P < 0.001, and ***P < 0.0001.

fig. S5E). In addition, the reduction of MDC1 protein expression in VGLL3-depleted U2OS cells could be reversed by supplementing with GFP-VGLL3 (Fig. 5D). While knockdown of KLHL15 could not rescue the MDC1 protein level (Fig. 5E) and 53BP1 focus formation (fig. S5F) in VGLL3-depleted cells, supporting the notion that VGLL3 modulates MDC1 expression and RNF8-RNF168 signaling in a KLHL15-independent fashion. We further determined the distinct contribution of MDC1 and KLHL15-CtIP in VGLL3regulated HR. KLHL15 depletion or hemagglutinin (HA)-MDC1 expression alone could significantly but not fully rescue the HR defect and RAD51 focus formation in VGLL3-depleted U2OS cells (Fig. 5, F and G, and fig. S5, G and H), while their combination could fully rescue these defects. Notably, MDC1 protein level exhibited no obvious alteration after depletion of VGLL1 or VGLL4 (fig. S5I), indicating that the effect of VGLL3 on MDC1 protein expression was not conserved among other VGLL family members. Collectively, these data support the notion that VGLL3 modulates MDC1 protein expression and RNF8-RNF168 signaling after DNA damage treatment in a KLHL15-CtIP axis-independent manner.

VGLL3 stabilizes MDC1 through promoting MDC1-USP7 but limiting MDC1-TRIP12 associations

We then explored how VGLL3 modulates MDC1 protein expression. We found that depletion of VGLL3 had no obvious effect on MDC1 mRNA expression, while MG132 addition could block the reduction of MDC1 protein in VGLL3-depleted cells (Fig. 6A), indicating that VGLL3 likely regulates MDC1 protein level through inhibiting its proteasome-mediated protein degradation. Consistently, VGLL3 knockdown caused an obvious increase of MDC1 ubiquitination (Fig. 6B). Ubiquitin-specific protease USP7 has been reported to physically associate with MDC1 to deubiquitinate and stabilize MDC1 (40). We then examined whether VGLL3 modulates USP7 protein expression. The result showed that knockdown of VGLL3 did not reduce USP7 protein level (Fig. 6C). VGLL3 is associated with both USP7 and MDC1 through Co-IP (Fig. 6D). VGLL3 also interacted with itself, mediated by its N-terminal fragment (Fig. 6E and fig. S6A). We then determined whether VGLL3 facilitates the MDC1-USP7 association. VGLL3-depleted 293T cells were transfected with Flag-USP7 and HA-MDC1 for Co-IP assay. The result showed that VGLL3 depletion impairs the MDC1-USP7 association (Fig. 6F). We further determined which domain of VGLL3 mediates its association with MDC1. The results revealed that deletion of H-rich motif (the $\triangle 6$ mutant) abrogated their association (Fig. 6G). Conversely, the C-terminal part of MDC1 mediated its association with VGLL3 (fig. S6, B and C). Moreover, unlike WT and $\triangle 1$ VGLL3 showing association with MDC1, the $\triangle 6$ mutant lost the ability to enhance the MDC1-USP7 interaction (Fig. 6H). Consequently, overexpression of WT or $\triangle 1$ VGLL3 but not the $\triangle 6$ mutant could efficiently reduce MDC1 ubiquitination (Fig. 6I). Meanwhile, we found that all VGLL3 deletion mutants still interact with USP7 (fig. S6D), suggesting that VGLL3 might associate with USP7 through multiple domains. Together, these results indicate that VGLL3 can stabilize MDC1 protein through promoting MDC1-USP7 association.

TRIP12 is a known ubiquitin E3 ligase for USP7, whose knockdown can stabilize USP7 (29). We found that TRIP12 knockdown could also rescue the MDC1 reduction in VGLL3-depleted cells, accompanying with an increase in USP7 protein abundance (Fig. 6J). We speculate that TRIP12 depletion might regulate MDC1 level through stabilizing

USP7, thereby shielding MDC1 from the ubiquitin-mediated proteasomal degradation. Unexpectedly, simultaneous depletion of USP7 and TRIP12 did not block the rescue effect (Fig. 6K), suggesting that TRIP12 possibly functions to directly promote MDC1 ubiquitination. To test that, we examined the association between TRIP12 and MDC1 or VGLL3 through Co-IP. The result showed that TRIP12 associates with MDC1 at C-terminal part but not VGLL3 (fig. S6, E to G). Moreover, we found that the level of MDC1 ubiquitination could be decreased by TRIP12 depletion but increased by USP7 depletion (fig. S6H). Simultaneous depletion of USP7 and TRIP12 could reduce the MDC1 ubiquitination to a similar extent as TRIP12 knockdown. These results suggest that TRIP12 likely promotes MDC1 ubiquitination and degradation, which could be reversed by USP7. Supportingly, we found that the depletion of TRIP12 could attenuate the up-regulation of MDC1 K48-linked polyubiquitination in siVGLL3-treated cells (Fig. 6L), indicating that TRIP12 can enhance MDC1 proteasomal degradation in those cells. Given that the C terminus of MDC1 associates with both VGLL3 and TRIP12, we then determined whether VGLL3 could competitively inhibit MDC1 association with TRIP12. Our Co-IP result showed that supplementing with VGLL3 could substantially inhibit the MDC1-TRIP12 association (fig. S6I). We also found that TRIP12 depletion could not inhibit VGLL3 ubiquitination (fig. S6J), in line with the fact that no association between them could be detected. Together, our data reveal that VGLL3 stabilizes MDC1 through promoting MDC1-USP7 while limiting MDC1-TRIP12 associations.

The E-rich and H-rich motifs of VGLL3 contribute to HR and tumor development

Given that the E-rich and H-rich motifs are necessary for VGLL3 to maintain CtIP and MDC1 stability, respectively, we then examined their contributions to the HR function of VGLL3. First, we determined their effects on RAD51, RPA, and MDC1 focus formation. U2OS cells stably expressing WT, $\Delta 2$, or $\Delta 6$ Flag-VGLL3 were depleted of endogenous VGLL3 followed by ETO treatment. Immunofluorescence assay showed that, although WT VGLL3 could fully rescue the reduced RAD51 and RPA focus formation in VGLL3depleted cells, $\Delta 2$ and $\Delta 6$ mutants only had a partial effect (Fig. 7, A and C). In addition, $\Delta 6$ mutant failed to reverse the decreased MDC1 focus formation in VGLL3-depleted cells (Fig. 7B), while both of WT and Δ2 VGLL3 exhibited an almost complete rescue effect, indicating that the E-rich motif or VGLL3 recruitment is not necessary for VGLL3-regulated MDC1 focus assembly. We further transfected siVGLL3 in U2OS-DR-GFP cells stably expressing WT, $\Delta 2$, or $\Delta 6$ Flag-VGLL3 for HR analysis. The result exhibited that, unlike WT VGLL3, $\Delta 2$ and $\Delta 6$ mutants could partially but not fully rescue the HR defect in VGLL3-depleted cells (Fig. 7D), supporting the notion that both motifs are required for optimal HR function of VGLL3.

To investigate how the E-rich and H-rich motifs of VGLL3 regulate tumor development and chemoresponse, MDA-MB-231 cells stably expressing WT, $\Delta 2$, or $\Delta 6$ Flag-VGLL3 were depleted of endogenous VGLL3 through lentivirus infection. CCK8 assays showed that VGLL3 depletion could decrease cellular growth and sensitize cells to ETO treatment (fig. S7, A to C). Complementing WT VGLL3 in VGLL3-depleted cells could rescue these defects (fig. S7, A to C), while $\Delta 2$ or $\Delta 6$ mutant only partially reversed the drug sensitivity. The cells were then transplanted into mammary fat pads of nude

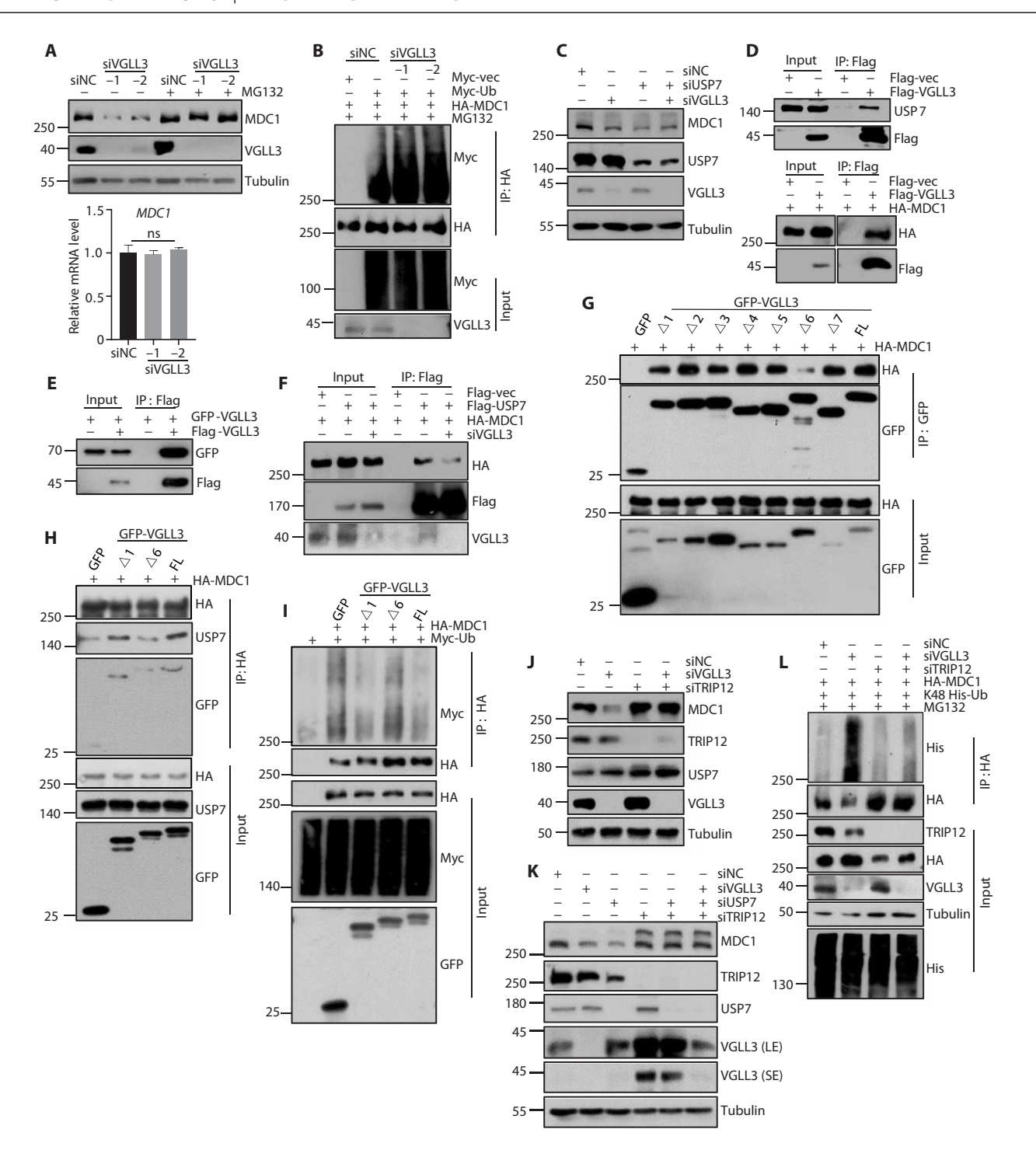


Fig. 6. VGLL3 stabilizes MDC1 through promoting MDC1-USP7 but limiting MDC1-TRIP12 associations. (**A**) VGLL3-depleted MDA-MB-231 cells were treated with MG132. MDC1 protein and mRNA levels were analyzed by IB (top) and qPCR (bottom). Data are presented as means \pm SEM from three experiments, unpaired *t* test. (**B**) VGLL3-depleted 293T cells were transfected with Myc-Ub and HA-MDC1. Thirty-six hours later, cells were treated with MG132 followed by denaturing IP using anti-HA beads. (**C**) MDA-MB-231 cells transfected with the indicated siRNAs were harvested for IB. (**D**) 293T cells transfected with Flag-VGLL3 (top) or Flag-VGLL3 and HA-MDC1 (bottom) were harvested for IP using anti-Flag beads. (**E**) 293T cells transfected with Flag-VGLL3 were harvested for IP using anti-Flag beads. (**F**) VGLL3-depleted 293T cells were transfected with Flag-USP7 and HA-MDC1. Cells were harvested for IP using anti-Flag beads. (**G**) 293T cells transfected with HA-MDC1 and GFP-VGLL3 deletions were harvested for IP using anti-GFP beads. (**H**) 293T cells cotransfected with HA-MDC1 and WT or Δ1 or Δ6 GFP-VGLL3 were harvested for IP using anti-HA beads. (**I**) 293T cells expressing WT or Δ1 or Δ6 GFP-VGLL3 were transfected with Myc-Ub and HA-MDC1. After 36 hours, cells were treated with MG132 followed by denaturing IP with anti-HA beads. (**J**) and **K**) MDA-MB-231 cells transfected with indicated siRNAs were harvested for IB. (**L**) 293T cells were treated with indicated siRNAs. Twenty-four hours later, cells were further transfected with SFB-CtIP and K48 HA-Ub. Thirty-six hours later, cells were treated with MG132 followed by denaturing IP with anti-HA beads.

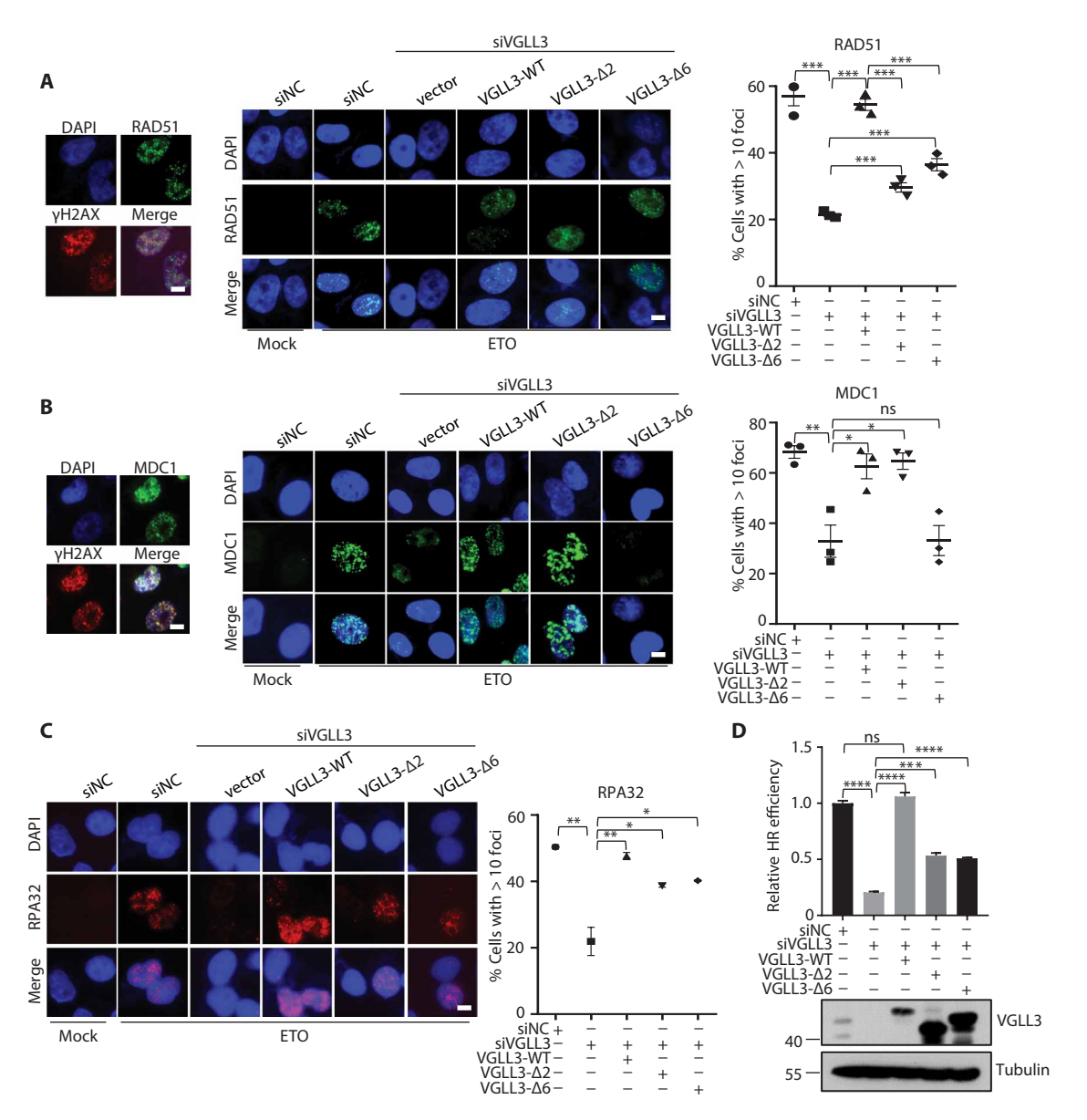


Fig. 7. The E-rich and H-rich motifs of VGLL3 are required for optimal HR. (A to C) U2OS cells stably expressing Flag, Flag-VGLL3, Flag-VGLL3- Δ 2, or Flag-VGLL3- Δ 6 were transfected with siVGLL3 or siNC for 72 hours. Cells were treated with ETO and cultured for 3 hours (for RAD51 and RPA32 IF) or 1 hour (for MDC1 IF), followed by IF with antibodies against RAD51 (A), MDC1 (B), and RPA32 (C). For (A) and (B), ETO-treated siNCs were also costained with anti-γH2AX antibody. Representative images are shown. Scale bars, 10 μm. Percentages of cells with >10 foci were quantified (more than 200 cells per replicate) (A and B: right; C: bottom). Data are presented as means ± SEM from three experiments, unpaired *t* test. (D) U2OS-DR-GFP cells stably expressing Flag, Flag-VGLL3- Δ 2, or Flag-VGLL3- Δ 6 were transfected with siNC or siVGLL3. After 24 hours, the cells were infected with I-Scel lentivirus. Percentage of GFP-positive cells was quantitated by fluorescence-activated cell sorting. A representative result from three individual experiments is shown. Data are presented as means ± SEM from three replicates per experiment. *P < 0.05, **P < 0.01, ***P < 0.001, and ****P < 0.0001.

mice with Matrigel. When the tumors became palpable, the mice were randomly grouped with or without ETO treatment. The result showed that VGLL3 depletion led to an obvious reduction in tumor volume, tumor weight, and Ki-67 level, which was reversed by supplementing with WT VGLL3 (Fig. 8, A to C and E), suggesting that VGLL3 is involved in tumor development. Moreover, VGLL3 depletion notably sensitized the xenografted tumor cells to ETO treatment, which was suppressed by supplementing with WT VGLL3 (Fig. 8, A to D). Compared to WT VGLL3, complementing with

either $\Delta 2$ or $\Delta 6$ mutant exhibited less effects in promoting tumor development and suppressing tumor chemosensitivity. In addition, ETO treatment resulted in decreased Ki67 signal and enhanced γ H2AX signal in VGLL3-deficient xenografts compared with shNC controls (Fig. 8, E and F, and fig. S7, D and E), which could be significantly reversed by complementing with WT VGLL3, while $\Delta 2$ or $\Delta 6$ mutant showed less effects compared to WT VGLL3. These results indicate a favorable therapeutic outcome by targeting the HR function of VGLL3. We also detected a reduced expression of CtIP

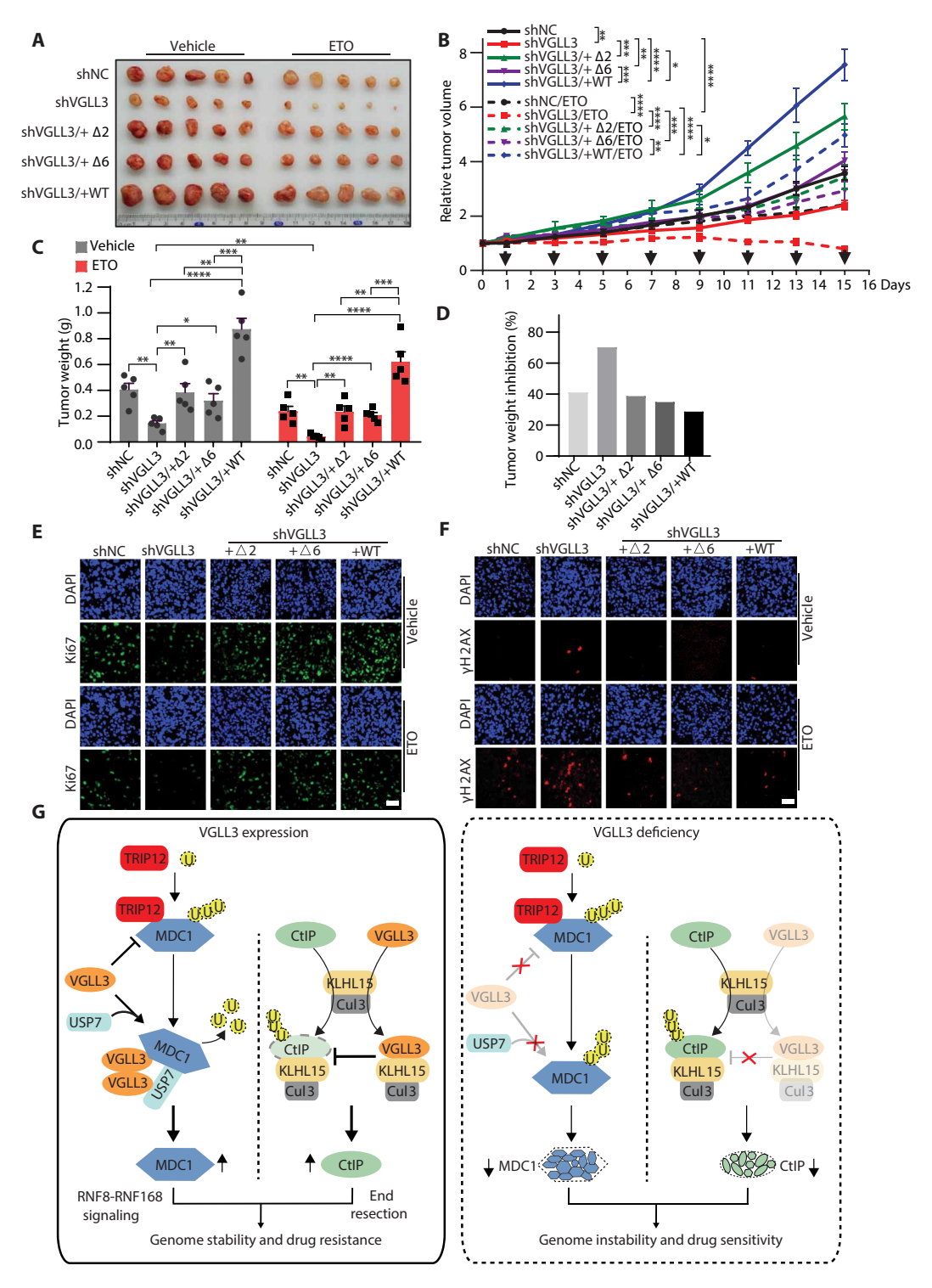


Fig. 8. The E-rich and H-rich motifs of VGLL3 contribute to tumor development. (**A** to **D**) MDA-MB-231 cells stably expressing $\Delta 2$ or $\Delta 6$ or WT VGLL3 were depleted of VGLL3 followed by xenograft assay (n=5 per group). Tumor graphs (A), tumor growth (B), tumor weight (C), and tumor weight inhibition rate (D) are shown. The arrow in (B) indicates each ETO treatment. (**E** and **F**) Representative histology stainings of Ki67 (E) and γH2AX (F) for tumor xenografts with indicated treatment. Scale bars, 100 μm. Data are presented as means \pm SEM, unpaired t test. (**G**) Model for VGLL3 in DDR and chemoresponse. *P < 0.05, **P < 0.01, ***P < 0.001, and ****P < 0.0001.

and MDC1 at protein but not mRNA level in VGLL3-depleted xenografts compared with the shNC controls (fig. S7, F and G). Complementing with WT VGLL3 increased the expression of both CtIP and MDC1 proteins, while $\Delta 2$ or $\Delta 6$ mutant only promotes MDC1 or CtIP protein level to a similar extent as WT, respectively (fig. S7, F and G). In line with these results, up-regulation of VGLL3 was associated with reduced overall survival in multiple patients with cancer, including ER-negative breast cancer, ovarian cancer, and gastric cancer, cataloged in public database (fig. S7, H and I), suggesting a potential significance of VGLL3 as a biomarker and therapeutic target for chemotherapy.

DISCUSSION

In this study, we have provided several lines of evidence to demonstrate that VGLL3 is a DDR factor to promote DSB repair, whose depletion can sensitize tumors to chemotherapy treatment. First, VGLL3 can be recruited to DNA damage sites in a PARylation- and CHD4-dependent manner. Second, VGLL3 stabilizes CtIP to promote DSB end resection. Third, VGLL3 stabilizes MDC1 to enhance RNF8-RNF168 signaling after ETO treatment through limiting TRIP12-mediated MDC1 ubiquitination and promoting USP7-mediated MDC1 deubiquitination. Fourth, tumor cells depleted of VGLL3 exhibits decreased HR and increased sensitivity to DSB-inducing agents. Last, VGLL3 depletion inhibits the growth of breast cancer cells and sensitizes the xenografts to chemotherapy treatment. Notably, the roles of VGLL3 in HR and MDC1 stabilization are not conserved among VGLL family members. Hence, our data support the notion that VGLL3 not only stabilizes CtIP to promote end resection but also stabilizes MDC1 to stimulate RNF8-RNF168 signalling, which synergistically enhance RAD51 focus formation after damage treatment, augmenting DSB repair (Fig. 8G). Notably, although VGLL3 depletion substantially impairs the recruitment of 53BP1 to damage sites, VGLL3 loss does not impair NHEJ, as shown in either NHEJ reporter assay or ICRF-193-induced cell killing assay. In line with that, recent studies showed that 53BP1 deficiency only causes a nonsignificant reduction in NHEJ (41), and canonical NHEJ may not strictly rely on 53BP1 (42).

CtIP is required for initial DSB end processing (14, 43), whose level is under sophisticated regulations by posttranslational modifications (16, 34, 44, 45). Among them, CUL3-KLHL15 ubiquitin ligase has been found to be important to govern the turnover of CtIP (35). Similar to the recently identified PACMP micropeptide (28), VGLL3 also associates with KLHL15 and can competitively inhibit the association of KLHL15-CtIP and protect CtIP from KLHL15-mediated ubiquitination. In addition, the modulation of VGLL3 on CtIP level is independent of PACMP. Our data show that depletion of either PACMP or VGLL3 shows no interacting effect on their expression, while depleting both can cause an additive inhibitory effect on the CtIP protein abundance. These data strongly suggest that CUL3-KLHL15-CtIP association can be coordinately regulated by distinct factors, ensuring proper CtIP protein level for optimal DNA end resection and HR repair when necessary.

While MDC1 has been shown to be ubiquitinated and degraded via the ubiquitin-proteasome system to facilitate its focus disassembly during DDR (46), it has a more durable residence in the damaged sites (20). Recently, the deubiquitinase ataxin-3 has been reported to counteract RNF4 activity at DSBs to negatively regulate MDC1 ubiquitination and premature removal (47). Here, our data indicate that VGLL3 can enhance MDC1 protein abundance through promoting

its association with USP7, which is known to efficiently deubiquitinate MDC1 (40). Given that VGLL3 and USP7 can both be recruited to DSB sites, and USP7-promoted MDC1 stabilization is potentiated by DNA damage (40), our finding suggests that VGLL3 likely has a potential to ensure a more robust MDC1-dependent signaling. In addition, MDC1 was found to interact with pre-ribosomal RNA for phase separation of DSB repair factors at DNA lesions (48). The role of VGLL3 in stabilizing MDC1 may promote the generation of an essential mediator platform for subsequent recruitment of multiple DDR factors to facilitate optimal DSB repair. In support with that, VGLL3 is required for efficient MDC1-dependent recruitment of RNF8, RNF168, and 53BP1. Consequently, VGLL3 depletion sensitizes cells to PARPi and DSB-causing agents.

We found that knockdown of the USP7 E3 ligase TRIP12 (36) can also rescue the MDC1 reduction in VGLL3-depleted cells, in the presence or absence of USP7 depletion. In addition, depletion of TRIP12 could reverse the up-regulated MDC1 K48 ubiquitination in VGLL3-depleted cells. The enhanced MDC1 K48 ubiquitination caused by USP7 depletion could be rescued by simultaneous depletion of TRIP12. These data suggest that TRIP12 can function independently of USP7 to promote MDC1 K48 ubiquitination and degradation, which could be largely reversed by USP7, in a manner analogous to their modulatory roles on RNF168 protein (21, 49). Notably, TRIP12 depletion could also increase VGLL3 protein abundance, although their association is not detected and TRIP12 loss failed to reduce VGLL3 ubiquitination. Nevertheless, how TRIP12 regulates VGLL3 expression deserves further exploration in the future.

Mouse VGLL3 was recently reported to undergo liquid-liquid phase separation to be incorporated into non-paraspeckle non-POU domain containing octamer binding protein (NONO) condensates in hepatic myofibroblasts through its E-rich motif (2). The disordered motif is conserved in human VGLL3, although the latter has less number of glutamate in that domain. Our data show that, unlike mouse VGLL3, human VGLL3 does not form obvious nuclear puncta when exogenously expressed in the U2OS and MDA-MB-231 cells under normal condition, whereas human VGLL3 can be recruited to DSBs through its E-rich motif in a PARylationdependent manner. Moreover, we found that the E-rich motif in VGLL3 mediates its association with CHD4, which is necessary for optimal VGLL3 recruitment at sites of damage. As a member of the SNF2 family of adenosine triphosphatase, CHD4 could be targeted to DSB sites in either RNF8-dependent or PARylation-dependent fashion (50–54) to promote chromatin relaxation in response to DNA damage. Consistent with the role of CHD4 in DSB repair, VGLL3 also promotes HR. In addition, we found that the E-rich domain is also required for VGLL3 self-interaction. Although the conserved C-terminal H-rich motif is not necessary for VGLL3 recruitment at sites of damage, it is required for VGLL3-MDC1 association, VGLL3-enhanced MDC1-USP7 interaction, and VGLL3-induced reduction in MDC1 ubiquitination. Through binding with MDC1, VGLL3 also competitively inhibit MDC1-TRIP12 association. Therefore, the unique E-rich and H-rich domains enable VGLL3 specific functions in stabilizing CtIP and MDC1, thereby synergistically promoting HR, which is not conserved among other VGLL family members. It is highly likely that VGLL3 may also regulate the stability of other DDR factors besides CtIP and MDC1, which remains to be identified in the future studies.

Similar to its homolog VGLL4 (12, 13), the expression levels of VGLL3 in multiple tumors are relatively lower in comparison with

paired pathologically normal tissues based on The Cancer Genome Atlas analysis. Given that MDC1 often functions as a tumor suppressor (24), it is plausible that the expression of VGLL3 that stabilizes MDC1 protein may serve to limit the initiation of those tumors. In addition, as a YAP target gene, VGLL3 mediates the transcriptional repression effect of YAP on ERα by competing with YAP/TAZ for binding to TEAD transcription factor and recruits the nuclear receptor co-repressor 2/silencing mediator for retinoid or thyroid-hormone (NCOR2/SMRT) repressor to the super-enhancer of ESR1 gene (7). However, although VGLL3 induction has a potential to suppress ERαdependent breast tumor growth, VGLL3 was recently found to function as a transcription co-activator to induce the expression of YAP-suppressed genes, which contributes to cancer cell survival and confers therapeutic resistance to TEAD-YAP blockade (11). Moreover, the role of VGLL3 in stabilizing CtIP and MDC1 at the protein level indicates that the functions of VGLL3 in tumor development and drug response are far more complex than expected, which deserves further studies.

Collectively, our findings identified an unexpected role of VGLL3 in DDR via stabilizing CtIP and MDC1. Given that DDR can protect tumor cells from genotoxic drug treatment, a better therapeutic outcome can be achieved by inhibition of VGLL3 DDR function and its association with TEAD.

MATERIALS AND METHODS

Cell culture and reagents

Human U2OS (osteosarcoma), MDA-MB-231 (triple-negative breast cancer), MCF7, SK-OV-3 (ovarian cancer), A375 (melanoma), and 293T cells were purchased from the American Type Culture Collection (Rockville, MD, USA). U2OS cells harboring a chromosomally integrated copy of the DR-GFP (55) or EJ5-GFP (56) reporter were provided by X. Xu. All cell lines were grown in Dulbecco's modified Eagle's medium (DMEM) at 37°C, 5% CO₂ with 10% fetal bovine serum if not specified. All cell lines were monitored regularly for their authenticity (Biowing Applied Biotechnology Corporation, Shanghai, China) and to be free of mycoplasma contamination. Cellular transfections with plasmids or small interfering RNA (siRNAs) were performed using VigoFect (Vigorous Biotechnology) or Lipofectamine RNAiMax (Invitrogen), respectively, following the manufacturer's instructions. All the siRNAs were obtained from GenePharma (Shanghai, China), and the sequences are listed in table S2.

Mice

Four-week-old female BALB/c nude mice were purchased from Vital River Laboratory Animal Technology Company (Beijing, China) and used for MDA-MB-231 xenografts. All mice were housed in pathogen-free animal facility with ad libitum access to food and water. All animal procedures were performed according to protocols approved by the Rules for Animal Experiments published by the Chinese Government (Beijing, China) and approved by the Research Ethics Committee of Beijing Institute of Genomics, China (2022S014).

Antibodies

Anti-CtIP [1:1000 dilution for Western blot (WB)] and anti-EXO1 (1:1000 dilution for WB) antibodies were purchased from Active Motif and Thermo Fisher Scientific, respectively. Anti-RPA32 (RPA2) (1:1000 dilution for WB), anti-RAD51 (1:1000 dilution for WB), anti- γ H2AX (1:1000 dilution for WB), and anti-VGLL4 (1:1000

dilution for WB) antibodies were purchased from Abcam. Anti-MRE11 (1:1000 dilution for WB) antibody was purchased from Novus Biologicals, respectively. Anti-KLHL15 (1:1000 dilution for WB) and anti-MDC1 (1:2000 dilution for WB) antibodies were purchased from Proteintech. Anti-CHD4 (1:1000 dilution for WB) antibody was purchased from Bioworld and Santa Cruz Biotechnology, respectively. The detailed information for antibodies is listed in table S3.

Plasmids

Human VGLL3 cDNA was cloned in pEGFP-C3 (Clontech) or pCMV5-Flag to generate eGFP or Flag fusion proteins. For generating deletion mutants, cDNA fragments of *vgll3* gene were PCR-amplified and cloned into pCMV5-Flag or pEGFP-C3, respectively. HA-CHD4 and pcDNA4TO-GFP-CHD4 were provided by S. Jackson and J. Lukas, respectively (*51*, *52*). The I-SceI lentivirus expression system (NOVO Bio, Shanghai) was from H. Wang. SFB-CtIP plasmid was from J. Wang. The pBabe-ER-AsiSI plasmid (*57*) was provided by G. Legube. Full-length and truncated HA-MDC1 plasmids as well as Flag-USP7 were provided by J. Yuan and L. Shi.

Laser microirradiation and imaging

Laser microirradiation was performed with a pulsed nitrogen laser (365 nm, 10-Hz pulse) as previously described (28). Briefly, cells were seeded on 35-mm glass bottom dishes (MatTek) overnight before being visualized with a Nikon Eclipse Ti-E inverted microscope equipped with a computer-controlled MicroPoint laser Ablation System (Photonics Instruments). The output of laser power was set to five pulses with 30% transmission. Time-lapse images of VGLL3 in live cells were taken under the same microscope, and the recruitment kinetics were analyzed with ImageJ software (National Institutes of Health). Recruitment intensity was analyzed using a macro written for ImageJ that calculated the ratio of intensity of a circumscribed laser spot A to the adjacent area B such that a radiommuno-focus unit (RFU) for each data collection point was calculated by the equation RFU = (A – C)/(B – C), where C is the background intensity of an unpopulated area of the image.

Generation of KO clones with CRISPR-Cas9

Three single guide RNAs (sgRNAs) targeting human VGLL3 were synthesized and cloned into an all-in-one pYSY-CMV-Cas9-U6gRNA-EF1a-Puro vector (Nanjing YSY Biotech, China) to generate the pYSY-Cas9-VGLL3-sgRNA-Puro plasmids. U2OS and MDA-MB-231 cells were transfected with the plasmid mixtures through a CUY21EditII electroporator (BEX Co. Ltd., Japan). Forty-eight hours later, the transfected cells were treated with puromycin (1.2 µg/ ml) for 3 days followed by single-cell seeding to generate KO clones, which were confirmed through immunoblotting and Sanger sequencing. The anti-VGLL3 polyclonal antibody was generated by immunizing New Zealand rabbits with two synthetic peptides (SCAEVMYHPQPYGASQ and DPSPWPGHNLHQTG) (residues 2 to 17 and 183 to 196 in VGLL3, respectively) conjugated to the carrier protein Keyhole Limpet Hemocyanin. Antisera were purified by immuno-affinity purification by GL Biochem, Shanghai. Antibodies specificity was verified by immunoblotting. The sgRNA targeting sequences were listed in table S2.

Co-IP and immunoblotting

Human embryonic kidney 293T cells were transfected with indicated plasmids. Forty-eight hours later, cells were lysed with Hepes

buffer [50 mM Hepes (pH 7.5), 150 mM NaCl, 1 mM EDTA, 1 mM EGTA, 10% glycerol, 1% Triton X-100, 25 mM NaF, and 10 µM ZnCl₂] containing protease inhibitors for 30 min. After the removal of cell debris by centrifugation at 12,000 rpm for 10 min, the supernatants were collected and incubated with appropriate antibody conjugated beads for 4 hours at 4°C. Beads were washed three times with Hepes buffer and boiled in 1x SDS loading buffer for 5 min. Samples were resolved by SDS-polyacrylamide gel electrophoresis (PAGE) followed by immunoblotting (IB) with the indicated antibodies.

Immunofluorescence

Cells were plated on coverslips in 35-mm dish. The next day, the cells were either untreated or treated with ETO and collected at the indicated time points. To detect 53BP1 and BRCA1 foci, cells were washed with phosphate-buffered saline (PBS), fixed in 4% paraformaldehyde (PFA) for 15 min, and permeabilized with 0.5% Triton X-100 for 10 min at room temperature (RT). To detect RPA, RAD51 RNF8 and RNF168 foci, cells were pre-extracted with 0.25 to 0.5% Triton X-100 (RPA for 25 min; RAD51/RNF8/RNF168 for 5 min) before fixation. Subsequently, cells were blocked with 5% bovine serum albumin (BSA) in PBS for 1 hour and incubated with primary antibodies (anti-RPA2, 1:1000; anti-RAD51, 1:100; anti-BRCA1, 1:200; anti-53BP1, 1:200; anti-RNF8, 1:100; and anti-RNF168, 1:100) overnight at 4°C. After washes with phosphate-buffered saline with 0.2% tween-20 (PBST), cells were incubated with Alexa Fluor 568- or Alexa Fluor 488-labeled secondary antibodies (Invitrogen) at RT for 45 min. After washing, the coverslips were mounted using mounting medium with 4',6-diamidino-2-phenylindole (Vector Laboratories). Images were acquired with a Leica DM5000 equipped with HCX PL S-APO 63 × 1.3 oil CS immersion objective (Leica) and processed with Adobe Photoshop 7.0. The percentage of cells with >10 RPA, RAD51, BRCA1, RNF8, RNF168, or 53BP1 foci was determined from three independent experiments. More than 150 cells were counted per experiment.

To detect the levels of DNA damage and cell proliferation in xenografted tumors, the xenografts were formalin-fixed and paraffinembedded. Sections (5 µm) on slides were dewaxed in xylene and then sequentially rehydrated in 100, 95, and 70% ethanol and PBS buffer. Antigen retrieval was performed in boiled pH 9.0 EDTA buffer (Zhong Shan JinQiao, Beijing, China) for 10 min. Sections were blocked with 1% BSA, 5% donkey serum, and 0.5% Triton X-100 in PBS buffer and then incubated overnight at 4°C with primary antibodies (yH2AX, 1:2000; Ki-67, 1:500). After washing, samples were incubated with Alexa Fluor 488-labeled secondary antibodies at RT for 1 hour. The percentage of $\gamma H2AX$ - or Ki-67-positive cells was determined from three independent tumors.

HR, NHEJ, and MMEJ assay

U2OS cells integrated with DR-GFP, EJ5-GFP, or EGFP-MMEJ cassettes were used in the analysis of HR or NHEJ or MMEJ efficiency, respectively, as previously (28). About 0.5×10^6 cells seeded in sixwell plates were transfected with the indicated siRNAs or plasmids and then infected with the I-SceI lentivirus harvested from 293T package cells. Two days later, the percentages of GFP-positive cells were analyzed by flow cytometry (BD FACSAria).

Cells were seeded into 96-well plates (4000 to 8000 cells per well) and allowed to adhere for 12 hours. The cells were then treated with EPI, ETO, or olaparib as indicated at 37°C. After treatments, cells were further incubated with the CCK8 reagent (DOJINDO) at 10% concentration in complete medium for 2 to 4 hours. Then, the absorbance at the wavelength of 465 nm was measured with the microplate reader. The survival of genotoxin-exposed cells was determined by relating the absorbance to that of an untreated control.

Clonogenic assay

Clonogenic assay was performed as previously described (28). Briefly, the cells were seeded in 6-cm dish for 24 hours and then treated with the indicated doses of CPT or ICRF-193 for 2 hours. After treatment, cells were further incubated with complete medium for about 2 weeks. Colonies were fixed and counted. The survival of genotoxin-exposed cells was determined by relating the cloning efficiency to that of an untreated control.

ChIP quantitative real-time PCR (ChIP-qPCR)

ChIP-qPCR was performed as previously described (58). Briefly, 1×10^6 DR-GFP U2OS cells with one copy of the DR-GFP gene stably integrated into its genome (59) were infected with either pLVx-Flag-VGLL3-WT or pLVx-Flag-VGLL3-Δ2 lentivirus. After I-SceI induction of DSBs, cells were crosslinked with 1% formaldehyde for 10 min at room temperature and quenched by the addition of glycine to a final concentration of 125 mM for 5 min. After washing twice with ice-cold PBS, the cells were collected by scraping. Pelleted cells were resuspended in 400 µl of lysis buffer [1% SDS, 10 mM EDTA, and 50 mM tris-HCl (pH 8.1)] in the presence of protease inhibitors and subjected to 15 cycles (high power, 30-s on and 30-s off) of sonication (Bioruptor, Diagenode) to generate chromatin fragments of 200 to 500 base pairs in length. After sonication, samples were diluted 10 times with buffer [1% Triton X-100, 2 mM EDTA, 20 mM tris-HCl (pH 8.1), and 150 mM NaCl] and centrifuged. Fifty microliters of supernatants was taken out as input. The remaining supernatants were immunoprecipitated using anti-Flag M2 beads at 4°C overnight. Beads were then washed sequentially with low-salt buffer [0.1% SDS, 1% Triton X-100, 2 mM EDTA, 20 mM tris-HCl (pH 8.1), and 150 mM NaCl], high-salt buffer [0.1% SDS, 1% Triton X-100, 2 mM EDTA, 20 mM tris-HCl (pH 8.1), and 500 mM NaCl], LiCl buffer [250 mM LiCl, 1% deoxycolic acid, 1 mM EDTA, and 10 mM tris-HCl (pH 8.1)], and TE [10 mM tris-HCl and 1 mM EDTA (pH 8.0)] before being $\,$ eluted with elution buffer (1% SDS, 5 mM EDTA, 20 mM tris-HCl (pH 8.1), and 50 mM NaCl]. Then, the pulled down chromatin complex together with input were decrosslinked in elution buffer containing proteinase K (0.1 mg/ml) at 65°C overnight before purification with a PCR purification kit (Zymo Research, D4033) and analyzed by qPCR. The enrichment of VGLL3 at I-Sce1-induced DSBs was plotted as percentage of input. The primer sequences were listed in table S2.

DNA end resection analysis

Genomic DNA extraction and preparation for the measurement of resection in mammalian cells were performed as previously described with some modifications (28, 60). Briefly, U2OS cells were infected with ER-AsiSI retrovirus harvested from 293T cells. The resulting U2OS cells stably expressing ER-AsiSI were transfected with siNC or siVGLL3. Forty-eight hours later, the cells were treated with or without 4-OHT (300 nM) (Sigma-Aldrich) for 6 hours to induce AsiSI-dependent DSBs. Cells were then harvested, and

genomic DNA was extracted by a Quick-DNA Microprep Kit (Zymo Research, D3020). For each sample, around 150 ng of extracted DNA was mock digested or digested with 20 units of BsrG1-HF (NEB) for 24 hours at 37°C. DNA end resection adjacent to the DSB1 (chromosome 1: 89231183) was measured by qPCR using Bio-Rad CFX96 TOUCH (Bio-Rad). The percentage of ssDNA was quantified using the equation of $100/(^2(\Delta \text{Ct}-1)+0.5)$. The primer sequences were listed in table S2.

Cell cycle

U2OS cells were harvested after the depletion of VGLL3 for 48 hours. Cells were washed twice with PBS and fixed in ice-cold 70% ethanol overnight. After treatment with ribonuclease (suspended in PBS, containing 0.2% Triton X-100 and 1% BSA) at room temperature for 20 min, cells were incubated with propidium iodide (5 $\mu g/ml)$ for 30 min in the dark followed by termination with PBS. Cell cycle distribution was analyzed by a FACSCalibur flow cytometer (BD Biosciences).

Micronucleus formation assay

Micronucleus formation assay was performed as described (61). Briefly, U2OS/MDA-MB-231 cells transfected with siNC or siVGLL3 were treated with bleomycin ($4\,\mu\text{g/ml}$) for 2 hours followed by incubating with cytochalasin B ($6\,\mu\text{g/ml}$) in complete medium for 48 hours. The cells were trypsinized and washed with PBS once and further treated with 0.075 M KCl for 20 min. Cells were then centrifuged to remove most hypotonic buffer and resuspended in the left-over buffer. Just before evaluation with a fluoresence microscope using a $40\times$ objective, $20\,\mu$ l of the cells was stained with acridine orange (final concentration was around 0.01%). Around 1000 cells with two nuclei per group were counted to calculate the micronuclei rate per experiment. The experiment was conducted with at least three biological replicates.

RNA extraction and reverse transcriptase qPCR

Cellular total RNA was isolated using TRIzol reagent following the instructions of the manufacturer (Invitrogen). Next, 2 µg of RNA was reverse-transcribed to cDNA using the High-Capacity cDNA Reverse Transcription Kit according to the manufacturer's instructions (Tiangen, KR106-02). Then, cDNA was diluted and subjected to real-time PCR with gene-specific primers using SYBR Green Realtime PCR Master Mix (Toyobo, QPK-201) and the Bio-Rad CFX96 TOUCH (Bio-Rad). All the primers for qPCR are listed in table S2.

GST pull-down assay

GST-CtIP^{CTD} was purified as previously described (28). Briefly, transformed BL21 cells were induced overnight with 0.2 mM isopropyl- β -D-thiogalactopyranoside, sonicated in NETN buffer [20 mM tris-HCl (pH 8.0), 200 mM NaCl, 0.5 mM EDTA, and 0.5% NP-40] with 1 mM phenylmethylsulfonyl fluoride and 1 mM dithiothreitol and then spun at 13,000g for 30 min at 4°C. The supernatant was incubated with the Glutathione Sepharose 4B beads (GE) for 4 hours. After washing, the bead-immobilized GST fusion proteins were stored in NETN buffer at 4°C. For GST-CtIP^{CTD} competition assay, 293T cells transfected with a fixed amount of GFP-KLHL15 and gradual increased amounts of WT or $\Delta 2$ Flag-VGLL3 were lysed in Hepes buffer [50 mM Hepes (pH 7.5), 150 mM NaCl, 1 mM EDTA, 1 mM EGTA, 10% glycerol, 1% Triton X-100, 25 mM NaF, and 10 μ M ZnCl₂]. The supernatants

were incubated with bead-immobilized GST-CtIP^{CTD} for 3 hours at 4°C. After washing with Hepes buffer, beads were boiled in SDS loading buffer for IB analysis.

Tandem affinity purification of S-Flag-SBP (SFB)-tagged VGLL3 complexes

293T cells expressing SFB-VGLL3 were crosslinked with 10 mM Dimethyl dithiobispropionimidate (DTBP) for 40 min on ice as previously described (62). The cells were then incubated with cytoplasm extraction buffer [10 mM tris-HCl (pH 8.0), 0.08% Triton X-100, 150 mM NaCl, 1 mM MgCl₂, and 10 mM ZnCl₂] on ice for 5 min followed by centrifuging at 500g for 5 min. The pellets were resuspended and incubated with NP-40 lysis buffer (150 mM NaCl, 1 mM EDTA, 50 mM NaF, 1% NP-40, and 10 mM NaH₂PO₄) with deoxyribonuclease I for about 40 min followed by centrifuging at 13,000g for 20 min. The supernatants were incubated with anti-Flag M2 beads overnight at 4°C. After washing with NP-40 lysis buffer, the bead-bound proteins were eluted with Flag peptide (200 µg/ml; Sigma-Aldrich) in buffer [50 mM tris-HCl and 150 mM NaCl (pH 7.4)]. The elutes were then incubated with S protein beads (EMD Millipore) for 1 hour at 4°C. After washing with buffer (20 mM tris-HCl, 100 mM NaCl, 1 mM EDTA, and 0.5% NP-40), the immunocomplexes were subjected to SDS-PAGE and visualized by silver staining. The indicated bands were excised and digested, and the peptides were analyzed by liquid chromatography tandem mass spectrometry on a ProteomeX-LTQ mass spectrometer (Thermo Fisher Scientific, Waltham, USA).

Xenograft experiment

Xenograft experiment was performed as previously described with some modifications (28). Briefly'5 \times 10⁶ MDA-MB-231 cells were mixed with matrigel (Corning) and injected into the mammary fat pads of 4- to 6-week-old female BALB/c nude mice. When tumor size reached about 5 mm in maximum diameter, the mice were randomized into test groups (day 0). ETO was dissolved in H₂O containing 5% dimethyl sulfoxide and 40% polyethylene glycol, molecular weight 300. ETO (10 mg/kg) or vehicle was given intraperitoneally every 2 days for six times. During the process, the size of xenografts was measured once every other day. Tumor volumes were calculated by equation of (length \times width²)/2. Tumor growth was normalized to volumes on day 0. Mice were euthanized on the indicated date. Tumors were removed, weighed, and photographed. The inhibition rate of tumor weight was calculated using the equation of $(1 - TWt/TWc) \times 100$ (TWt and TWc are the mean tumor weight of treated and control groups, respectively).

Quantification and statistical analysis

All statistical calculations were performed using GraphPad Prism v.8.0 or Excel. One-way or two-way analysis of variance (ANOVA) was used to analyze statistical differences between multiple-group comparisons, and all other statistics were evaluated by two-sided Student's t test unless otherwise noted in the figure legends. Quantitative data were presented as means \pm SD or SEM. All the experiments were generally conducted with at least three biological replicates unless otherwise noted in the figure legends. Differences were considered significant at *P < 0.05, **P < 0.01, ***P < 0.001, and ****P < 0.0001.

Supplementary Materials

The PDF file includes:

Figs. S1 to S7 Tables S2 and S3 Legend for table S1

Other Supplementary Material for this manuscript includes the following:

REFERENCES AND NOTES

- N. Yamaguchi, Multiple roles of vestigial-like family members in tumor development. Front. Oncol. 10, 1266 (2020).
- Y. Horii, S. Matsuda, C. Toyota, T. Morinaga, T. Nakaya, S. Tsuchiya, M. Ohmuraya, T. Hironaka, R. Yoshiki, K. Kasai, Y. Yamauchi, N. Takizawa, A. Nagasaka, A. Tanaka, H. Kosako, M. Nakaya, VGLL3 is a mechanosensitive protein that promotes cardiac fibrosis through liquid-liquid phase separation. *Nat. Commun.* 14, 550 (2023).
- E. Salichs, A. Ledda, L. Mularoni, M. M. Alba, S. de la Luna, Genome-wide analysis of histidine repeats reveals their role in the localization of human proteins to the nuclear speckles compartment. PLOS Genet. 5, e1000397 (2009).
- Y. Liang, L. C. Tsoi, X. Xing, M. A. Beamer, W. R. Swindell, M. K. Sarkar, C. C. Berthier, P. E. Stuart, P. W. Harms, R. P. Nair, J. T. Elder, J. J. Voorhees, J. M. Kahlenberg, J. E. Gudjonsson, A gene network regulated by the transcription factor VGLL3 as a promoter of sex-biased autoimmune diseases. *Nat. Immunol.* 18, 152–160 (2017).
- A. C. Billi, M. Gharaee-Kermani, J. Fullmer, L. C. Tsoi, B. D. Hill, D. Gruszka, J. Ludwig, X. Xing, S. Estadt, S. J. Wolf, S. M. Rizvi, C. C. Berthier, J. B. Hodgin, M. A. Beamer, M. K. Sarkar, Y. Liang, R. Uppala, S. Shao, C. Zeng, P. W. Harms, M. E. Verhaegen, J. J. Voorhees, F. Wen, N. L. Ward, A. A. Dlugosz, J. M. Kahlenberg, J. E. Gudjonsson, The female-biased factor VGLL3 drives cutaneous and systemic autoimmunity. JCl Insight 4, e127291 (2019).
- Y. Takakura, N. Hori, N. Terada, M. Machida, N. Yamaguchi, H. Takano, N. Yamaguchi, VGLL3 activates inflammatory responses by inducing interleukin-1α secretion. FASEB J. 35, e21996 (2021).
- S. Ma, T. Tang, G. Probst, A. Konradi, C. Jin, F. Li, J. Silvio Gutkind, X.-D. Fu, K.-L. Guan, Transcriptional repression of estrogen receptor alpha by YAP reveals the Hippo pathway as therapeutic target for ER⁺ breast cancer. *Nat. Commun.* 13, 1061 (2022).
- N. Hori, Y. Takakura, A. Sugino, S. Iwasawa, K. Nomizo, N. Yamaguchi, H. Takano, N. Yamaguchi, Vestigial-like family member 3 stimulates cell motility by inducing high-mobility group AT-hook 2 expression in cancer cells. J. Cell. Mol. Med. 26, 2686–2697 (2022).
- N. Hori, K. Okada, Y. Takakura, H. Takano, N. Yamaguchi, N. Yamaguchi, Vestigial-like family member 3 (VGLL3), a cofactor for TEAD transcription factors, promotes cancer cell proliferation by activating the Hippo pathway. *J. Biol. Chem.* 295, 8798–8807 (2020).
- R. Haque, J. Lee, J.-Y. Chung, H.-Y. Shin, H.-Y. Kim, J.-H. Kim, J. W. Yun, E.-S. Kang, VGLL3 expression is associated with macrophage infiltration and predicts poor prognosis in epithelial ovarian cancer. *Front. Oncol.* 13, 1152991 (2023).
- Y. Sun, L. Hu, Z. Tao, G. K. Jarugumilli, H. Erb, A. Singh, Q. Li, J. L. Cotton, P. Greninger, R. K. Egan, Y. Tony Ip, C. H. Benes, J. Che, J. Mao, X. Wu, Pharmacological blockade of TEAD-YAP reveals its therapeutic limitation in cancer cells. *Nat. Commun.* 13, 6744 (2022).
- S. Jiao, H. Wang, Z. Shi, A. Dong, W. Zhang, X. Song, F. He, Y. Wang, Z. Zhang, W. Wang, X. Wang, T. Guo, P. Li, Y. Zhao, H. Ji, L. Zhang, Z. Zhou, A peptide mimicking VGLL4 function acts as a YAP antagonist therapy against gastric cancer. *Cancer Cell* 25, 166–180 (2014).
- W. Zhang, Y. Gao, P. Li, Z. Shi, T. Guo, F. Li, X. Han, Y. Feng, C. Zheng, Z. Wang, F. Li, H. Chen, Z. Zhou, L. Zhang, H. Ji, VGLL4 functions as a new tumor suppressor in lung cancer by negatively regulating the YAP-TEAD transcriptional complex. *Cell Res.* 24, 331–343 (2014).
- R. Scully, A. Panday, R. Elango, N. A. Willis, DNA double-strand break repair-pathway choice in somatic mammalian cells. *Nat. Rev. Mol. Cell Biol.* 20, 698–714 (2019).
- L. S. Symington, J. Gautier, Double-strand break end resection and repair pathway choice.
 Annu. Rev. Genet. 45, 247–271 (2011).
- F. Zhao, W. Kim, J. A. Kloeber, Z. Lou, DNA end resection and its role in DNA replication and DSB repair choice in mammalian cells. Exp. Mol. Med. 52, 1705–1714 (2020).
- G. S. Stewart, B. Wang, C. R. Bignell, A. M. R. Taylor, S. J. Elledge, MDC1 is a mediator of the mammalian DNA damage checkpoint. *Nature* 421, 961–966 (2003).
- Z. Lou, K. Minter-Dykhouse, S. Franco, M. Gostissa, M. A. Rivera, A. Celeste, J. P. Manis, J. van Deursen, A. Nussenzweig, T. T. Paull, F. W. Alt, J. Chen, MDC1 maintains genomic stability by participating in the amplification of ATM-dependent DNA damage signals. *Mol. Cell* 21, 187–200 (2006).
- M. Stucki, J. A. Clapperton, D. Mohammad, M. B. Yaffe, S. J. Smerdon, S. P. Jackson, MDC1 directly binds phosphorylated histone H2AX to regulate cellular responses to DNA double-strand breaks. Cell 123, 1213–1226 (2005).

- C. Lukas, F. Melander, M. Stucki, J. Falck, S. Bekker-Jensen, M. Goldberg, Y. Lerenthal,
 S. P. Jackson, J. Bartek, J. Lukas, Mdc1 couples DNA double-strand break recognition by Nbs1 with its H2AX-dependent chromatin retention. *EMBO J.* 23, 2674–2683 (2004).
- T. Gudjonsson, M. Altmeyer, V. Savic, L. Toledo, C. Dinant, M. Grofte, J. Bartkova, M. Poulsen, Y. Oka, S. Bekker-Jensen, N. Mailand, B. Neumann, J. K. Heriche, R. Shearer, D. Saunders, J. Bartek, J. Lukas, C. Lukas, TRIP12 and UBR5 suppress spreading of chromatin ubiquitylation at damaged chromosomes. *Cell* 150, 697–709 (2012).
- M. Tang, S. Li, J. Chen, Ubiquitylation in DNA double-strand break repair. DNA Repair 103, 103129 (2021).
- S. Nowsheen, K. Aziz, A. Aziz, M. Deng, B. Qin, K. Luo, K. B. Jeganathan, H. Zhang, T. Liu, J. Yu, Y. Deng, J. Yuan, W. Ding, J. M. van Deursen, Z. Lou, L3MBTL2 orchestrates ubiquitin signalling by dictating the sequential recruitment of RNF8 and RNF168 after DNA damage. *Nat. Cell Biol.* 20, 455–464 (2018).
- S. E. Ruff, S. K. Logan, M. J. Garabedian, T.T. Huang, Roles for MDC1 in cancer development and treatment. *DNA Repair* 95, 102948 (2020).
- J. Bartkova, Z. Horejsi, M. Sehested, J. M. Nesland, E. Rajpert-De Meyts, N. E. Skakkebaek, M. Stucki, S. Jackson, J. Lukas, J. Bartek, DNA damage response mediators MDC1 and 53BP1: Constitutive activation and aberrant loss in breast and lung cancer, but not in testicular germ cell tumours. Oncogene 26, 7414–7422 (2007).
- R. Xie, Z. Yan, J. Jing, Y. Wang, J. Zhang, Y. Li, X. Liu, X. Yu, C. Wu, Functional defects of cancer-associated MDC1 mutations in DNA damage repair. *DNA Repair (Amst)* 114, 103330 (2022).
- T. Liu, J. Huang, DNA end resection: Facts and mechanisms. Genomics Proteomics Bioinformatics 14, 126–130 (2016).
- C. Zhang, B. Zhou, F. Gu, H. Liu, H. Wu, F. Yao, H. Zheng, H. Fu, W. Chong, S. Cai, M. Huang, X. Ma, Z. Guo, T. Li, W. Deng, M. Zheng, Q. Ji, Y. Zhao, Y. Ma, Q.-E. Wang, T.-S. Tang, C. Guo, Micropeptide PACMP inhibition elicits synthetic lethal effects by decreasing CtIP and poly(ADP-ribosyl)ation. *Mol. Cell* 82, 1297–1312.e8 (2022).
- X. Liu, X. Yang, Y. Li, S. Zhao, C. Li, P. Ma, B. Mao, Trip12 is an E3 ubiquitin ligase for USP7/ HAUSP involved in the DNA damage response. FEBS Lett. 590, 4213–4222 (2016).
- L. Izhar, B. Adamson, A. Ciccia, J. Lewis, L. Pontano-Vaites, Y. Leng, A. C. Liang, T. F. Westbrook, J. W. Harper, S. J. Elledge, A systematic analysis of factors localized to damaged chromatin reveals PARP-dependent recruitment of transcription factors. *Cell Rep.* 11, 1486–1500 (2015).
- R. Smith, H. Sellou, C. Chapuis, S. Huet, G. Timinszky, CHD3 and CHD4 recruitment and chromatin remodeling activity at DNA breaks is promoted by early poly(ADP-ribose)dependent chromatin relaxation. *Nucleic Acids Res.* 46, 6087–6098 (2018).
- H. Sellou, T. Lebeaupin, C. Chapuis, R. Smith, A. Hegele, H. R. Singh, M. Kozlowski,
 Bultmann, A. G. Ladurner, G. Timinszky, S. Huet, The poly(ADP-ribose)-dependent chromatin remodeler Alc1 induces local chromatin relaxation upon DNA damage. *Mol. Biol. Cell* 27, 3791–3799 (2016).
- M. Xing, M. Yang, W. Huo, F. Feng, L. Wei, W. Jiang, S. Ning, Z. Yan, W. Li, Q. Wang, M. Hou, C. Dong, R. Guo, G. Gao, J. Ji, S. Zha, L. Lan, H. Liang, D. Xu, Interactome analysis identifies a new paralogue of XRCC4 in non-homologous end joining DNA repair pathway. *Nat. Commun.* 6, 6233 (2015).
- M. Gao, G. Guo, J. Huang, J. A. Kloeber, F. Zhao, M. Deng, X. Tu, W. Kim, Q. Zhou, C. Zhang, P. Yin, K. Luo, Z. Lou, USP52 regulates DNA end resection and chemosensitivity through removing inhibitory ubiquitination from CtIP. Nat. Commun. 11, 5362 (2020).
- L. P. Ferretti, S.-F. Himmels, A. Trenner, C. Walker, C. von Aesch, A. Eggenschwiler,
 O. Murina, R. I. Enchev, M. Peter, R. Freire, A. Porro, A. A. Sartori, Cullin3-KLHL15 ubiquitin ligase mediates CtlP protein turnover to fine-tune DNA-end resection. *Nat. Commun.* 7, 12628 (2016).
- L. Lafranchi, H. R. de Boer, E. G. de Vries, S.-E. Ong, A. A. Sartori, M. A. van Vugt, APC/C(Cdh1) controls CtIP stability during the cell cycle and in response to DNA damage. EMBO J. 33, 2860–2879 (2014).
- M. S. Luijsterburg, D. Typas, M.-C. Caron, W. W. Wiegant, D. van den Heuvel, R. A. Boonen, A. M. Couturier, L. H. Mullenders, J.-Y. Masson, H. J. E. van Attikum, A PALB2-interacting domain in RNF168 couples homologous recombination to DNA break-induced chromatin ubiquitylation. eLife 6, e20922 (2017).
- S. Nakada, R. M. Yonamine, K. Matsuo, RNF8 regulates assembly of RAD51 at DNA double-strand breaks in the absence of BRCA1 and 53BP1. Cancer Res. 72, 4974–4983 (2012).
- D. Zong, S. Adam, Y. Wang, H. Sasanuma, E. Callén, M. Murga, A. Day, M. J. Kruhlak, N. Wong, M. Munro, A. R. Chaudhuri, B. Karim, B. Xia, S. Takeda, N. Johnson, D. Durocher, A. Nussenzweig, BRCA1 haploinsufficiency is masked by RNF168-mediated chromatin ubiquitylation. 73, 1267–1281.e7 (2019).
- D. Su, S. Ma, L. Shan, Y. Wang, Y. Wang, C. Cao, B. Liu, C. Yang, L. Wang, S. Tian, X. Ding, X. Liu, N. Yu, N. Song, L. Liu, S. Yang, Q. Zhang, F. Yang, K. Zhang, L. Shi, Ubiquitin-specific protease 7 sustains DNA damage response and promotes cervical carcinogenesis. *J. Clin. Invest.* 128, 4280–4296 (2018).

SCIENCE ADVANCES | RESEARCH ARTICLE

- W. Feng, D. A. Simpson, J. Carvajal-Garcia, B. A. Price, R. J. Kumar, L. E. Mose, R. D. Wood, N. Rashid, J. E. Purvis, J. S. Parker, D. A. Ramsden, G. P. Gupta, Genetic determinants of cellular addiction to DNA polymerase theta. *Nat. Commun.* 10, 4286 (2019).
- M. B. Rother, S. Pellegrino, R. Smith, M. Gatti, C. Meisenberg, W. W. Wiegant, M. S. Luijsterburg, R. Imhof, J. A. Downs, A. C. O. Vertegaal, S. Huet, M. Altmeyer, H. van Attikum, CHD7 and 53BP1 regulate distinct pathways for the re-ligation of DNA double-strand breaks. *Nat. Commun.* 11, 5775 (2020).
- Z. You, L. Z. Shi, Q. Zhu, P. Wu, Y. W. Zhang, A. Basilio, N. Tonnu, I. M. Verma, M. W. Berns, T. Hunter, CtlP links DNA double-strand break sensing to resection. *Mol. Cell* 36, 954–969 (2009)
- J. Han, L. Wan, G. Jiang, L. Cao, F. Xia, T. Tian, X. Zhu, M. Wu, M. S. Y. Huen, Y. Wang, T. Liu,
 J. Huang, ATM controls the extent of DNA end resection by eliciting sequential posttranslational modifications of CtIP. Proc. Natl. Acad. Sci. U.S.A. 118, e2022600118 (2021).
- R. Anand, L. Ranjha, E. Cannavo, P. Cejka, Phosphorylated CtlP functions as a co-factor of the MRE11-RAD50-NBS1 endonuclease in DNA end resection. *Mol. Cell* 64, 940–950 (2016)
- W. Shi, Z. Ma, H. Willers, K. Akhtar, S. P. Scott, J. Zhang, S. Powell, J. Zhang, Disassembly of MDC1 foci is controlled by ubiquitin-proteasome-dependent degradation. *J. Biol. Chem.* 283, 31608–31616 (2008).
- A. Pfeiffer, M. S. Luijsterburg, K. Acs, W. W. Wiegant, A. Helfricht, L. K. Herzog, M. Minoia, C. Bottcher, F. A. Salomons, H. van Attikum, N. P. Dantuma, Ataxin-3 consolidates the MDC1-dependent DNA double-strand break response by counteracting the SUMOtargeted ubiquitin ligase RNF4. *EMBO J.* 36, 1066–1083 (2017).
- X. Gai, D. Xin, D. Wu, X. Wang, L. Chen, Y. Wang, K. Ma, Q. Li, P. Li, X. Yu, Pre-ribosomal RNA reorganizes DNA damage repair factors in nucleus during meiotic prophase and DNA damage response. Cell Res. 32, 254–268 (2022).
- M. Brunet, C. Vargas, D. Larrieu, J. Torrisani, M. Dufresne, E3 ubiquitin ligase TRIP12: Regulation, structure, and physiopathological functions. *Int. J. Mol. Sci.* 21, 8515 (2020).
- M. S. Luijsterburg, K. Acs, L. Ackermann, W. W. Wiegant, S. Bekker-Jensen, D. H. Larsen, K. K. Khanna, H. van Attikum, N. Mailand, N. P. Dantuma, A new non-catalytic role for ubiquitin ligase RNF8 in unfolding higher-order chromatin structure. *EMBO J.* 31, 2511–2527 (2012).
- D. H. Larsen, C. Poinsignon, T. Gudjonsson, C. Dinant, M. R. Payne, F. J. Hari, J. M. Rendtlew Danielsen, P. Menard, J. C. Sand, M. Stucki, C. Lukas, J. Bartek, J. S. Andersen, J. Lukas, The chromatin-remodeling factor CHD4 coordinates signaling and repair after DNA damage. *J. Cell Biol.* 190, 731–740 (2010).
- S. E. Polo, A. Kaidi, L. Baskcomb, Y. Galanty, S. P. Jackson, Regulation of DNA-damage responses and cell-cycle progression by the chromatin remodelling factor CHD4. *EMBO J.* 29, 3130–3139 (2010).
- G. Smeenk, W. W. Wiegant, H. Vrolijk, A. P. Solari, A. Pastink, H. van Attikum, The NuRD chromatin-remodeling complex regulates signaling and repair of DNA damage. *J. Cell Biol.* 190, 741–749 (2010).
- M.-R. Pan, H.-J. Hsieh, H. Dai, W.-C. Hung, K. Li, G. Peng, S.-Y. Lin, Chromodomain helicase DNA-binding protein 4 (CHD4) regulates homologous recombination DNA repair, and its deficiency sensitizes cells to poly(ADP-ribose) polymerase (PARP) inhibitor treatment. *J. Biol. Chem.* 287, 6764–6772 (2012).

- B. Xia, Q. Sheng, K. Nakanishi, A. Ohashi, J. Wu, N. Christ, X. Liu, M. Jasin, F. J. Couch,
 D. M. Livingston, Control of BRCA2 cellular and clinical functions by a nuclear partner,
 PALB2. Mol. Cell 22. 719–729 (2006).
- A. Gunn, N. Bennardo, A. Cheng, J. M. Stark, Correct end use during end joining of multiple chromosomal double strand breaks is influenced by repair protein RAD50, DNA-dependent protein kinase DNA-PKcs, and transcription context. *J. Biol. Chem.* 286, 42470–42482 (2011).
- J. S. Iacovoni, P. Caron, I. Lassadi, E. Nicolas, L. Massip, D. Trouche, G. Legube, Highresolution profiling of γH2AX around DNA double strand breaks in the mammalian genome. EMBO J. 29, 1446–1457 (2010).
- Y. Yang, Z. Liu, F. Wang, P. Temviriyanukul, X. Ma, Y. Tu, L. Lv, Y.-F. Lin, M. Huang, T. Zhang, H. Pei, B. P. C. Chen, J. G. Jansen, N. de Wind, P. L. Fischhaber, E. C. Friedberg, T.-S. Tang, C. Guo, FANCD2 and REV1 cooperate in the protection of nascent DNA strands in response to replication stress. *Nucleic Acids Res.* 43, 8325–8339 (2015).
- H. Pei, L. Zhang, K. Luo, Y. Qin, M. Chesi, F. Fei, P. L. Bergsagel, L. Wang, Z. You, Z. Lou, MMSET regulates histone H4K20 methylation and 53BP1 accumulation at DNA damage sites. *Nature* 470, 124–128 (2011).
- Y. Zhou, P. Caron, G. Legube, T. T. Paull, Quantitation of DNA double-strand break resection intermediates in human cells. *Nucleic Acids Res.* 42, e19 (2014).
- M. Huang, B. Zhou, J. Gong, L. Xing, X. Ma, F. Wang, W. Wu, H. Shen, C. Sun, X. Zhu, Y. Yang, Y. Sun, Y. Liu, T. S. Tang, C. Guo, RNA-splicing factor SART3 regulates translesion DNA synthesis. *Nucleic Acids Res.* 46, 4560–4574 (2018).
- L. Lv, F. Wang, X. Ma, Y. Yang, Z. Wang, H. Liu, X. Li, Z. Liu, T. Zhang, M. Huang,
 E. C. Friedberg, T.-S. Tang, C. Guo, Mismatch repair protein MSH2 regulates translesion
 DNA synthesis following exposure of cells to UV radiation. *Nucleic Acids Res.* 41, 10312–10322 (2013).

Acknowledgments: We thank G. Legube, L. Zhang, H. Wang, L. Shi, J. Yuan, J. Wang, W. Zhu, P. Ma, and X. Xu for reagents; Y. Zhao for proofreading; and laboratory members B. Zhou, Y. Sun, H. Li, Y. Liu, and L. Lv for project assistance. Funding: This work was supported by grants from the National Natural Science Foundation of China (82341006 and 82330090 to C.G., 82030033 and 81921006 and 92254301 to T.T., 82103081 to Z.F., and 32070780 to H.L.), the Beijing Natural Science Foundation (IS23071 to C.G.), the Postdoctoral Research Foundation of China (2021 M703206 to X.M.), and the State Key Laboratory of Membrane Biology. Author contributions: Conceptualization: C.G. and T.-S.T. Methodology: W.W., Z.F., H.F., and X. Ma. Investigation: W.W., Z.F., H.F., X. Ma, D.W., H.L., C.Z., H.Z., Y.Y., H.W., X.Mia., R.A., and Y.G. Visualization: W.W., Z.F., H.F., and X. Ma. Supervision: C.G. and T.-S.T. Writing—original draft: W.W. and C.G. Writing—review and editing: C.G. and T.-S.T. Competing interests: The authors declare that they have no competing interests. Data and materials availability: All data needed to evaluate the conclusions in the paper are present in the paper and/or the Supplementary Materials.

Submitted 23 June 2024 Accepted 4 September 2024 Published 9 October 2024 10.1126/sciadv.adr2643